INVESTIGATION OF MAGNETIC PROPERTIES OF $Ba_4Ni_{2-x}Zn_xFe_{36}O_{60}$ HEXAFERRITES

A Dissertation Submitted to Department of Physics, Bangladesh University of Engineering & Technology, Dhaka, in the Partial Fulfillment for Master of Philosophy in Physics

SUBMITTED BY

SANJOY KUMAR NANDI

ROLL NO. : 040814021F
SESSION : APRIL 2008

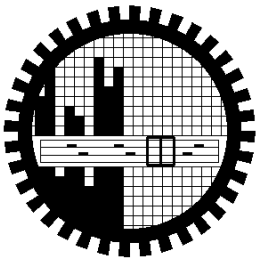

DEPARTMENT OF PHYSICS
BANGLADESH UNIVERSITY OF ENGINEERING & TECHNOLOGY
DHAKA-1000, BANGLADESH

CANDIDATE'S DECLARATION

It is hereby declared that this thesis or any part of it has not been submitted elsewhere for the award of any degree or diploma.

Sanjoy Kumar Nandi

Dedicated
to my
Late Grandfather
&
Late Grandmother

ABSTRACT

$Ba_4Ni_{2-x}Zn_xFe_{36}O_{60}$ *(0.0≤x≤1.2 with a step 0.2*) were prepared by conventional solid state reaction technique. Stoichiometric amounts of the $BaCO_3$, Fe_2O_3, NiO and ZnO were milled for12 h. After milling, compositions were subjected to sintering wherein it was controlled at 900°C and sintered powder was crushed into fine powder. The prepared fine powder was pressed into pellets and sintered at 1250, 1300 and 1350°C for 6 h. The X-ray diffraction (XRD) patterns for different compositions were analyzed. This analysis and the comparison of obtained XRD patterns with previously reported XRD patterns of U-type hexaferrites confirm the formation of the proper phase. The lattice parameters ά*a' and* άcô and c/a ratio for all samples are calculated. The value of lattice parameters are close to the usual values of a=5.88 Å and c=113 Å for U-type hexaferrite. There is an increase in lattice parameters are observed due to Zn substitution. The increase in lattice parameters with increasing Zn content can be explained on the basis of the ionic radii. The ionic radii of the cations used in $Ba_4Ni_{2-x}Zn_xFe_{36}O_{60}$ are 0.83Å (Ni^{2+}), 0.88Å (Zn^{2+}) and 0.69Å (Fe^{3+}). Since the ionic radius of Ni^{2+} is less than that of the Zn^{2+}, increase in lattice constant with the increase in *Zn* substitution is expected. The experimental density (d_{exp}) of the samples is observed to be increasing with increasing Zn content. This increase in density with increasing Zn content can be explained on the basis of the atomic weight. Since, the atomic weight of *Ni* (47.88 amu) is less than that of Zn (65.39 amu) therefore, increase of the density is expected. Structural and surface morphology were studied by the high resolution optical microscope (Olympus DP-70) for different compositions. The micrographs show that grain size increases with Zn content. The ac magnetic properties of the hexaferrites are characterized within the frequency range 0.1-120MHz. The real part (μ') of the complex permeability $\mu^* = \mu' - i\mu''$ for different compositions indicates that μ' decreases with increase in frequency. The decreasing trend in permeability μ' with frequency is a general phenomenon and is ascribed to the limited speed of spin and domain wall movement (displacement/ rotation) in the samples. In general, multiple resonances are more prominently observed in μ' spectrum of U-type hexaferrites. But weak resonance peaks were found due to domain wall motion for all sample within measured range of frequency. It is observed that permeability increases for

all samples as the sintering temperature increases from 1250 to 1300°C and above 1300°C the permeability decreases. The reason behind this is the samples being heated at higher temperature contain increasing number of pores within the grain which results in decrease in permeability. The observed increase of saturation magnetization (M_s) with Zn content is due to the fact that the diamagnetic Zn^{2+} cation takes the position on the spin-down and tetrahedral sites of T- and S-blocks. In order to explain this lower value of saturation above x=1 can be explained by local spin canting with a magnetic component along the hexagonal c-axis.

The variation of dielectric constant (ε) of $Ba_4Ni_{2-x}Zn_xFe_{36}O_{60}$ hexaferrites with frequency (1-100kHz) indicates that the dielectric constant decreases with increasing frequency and then reaches almost constant value due to the fact that beyond a certain frequency of external alternating field, the electron exchange between Fe^{+2} *and* Fe^{+3} cannot follow the alternating field. The addition of Zn^{2+} ions seems to disturb this equilibrium and could reduce the hopping conduction in the sample. On the other hand, Zn is also volatile in nature and some percentage of it escapes during sintering leaving some vacancies in the structure. The evaporation of Zn ions during sintering process may increase the number of Fe^{2+} ions at these sites, which in turn lead to an increase in hopping conduction.

ACKNOWLEDMENTS

First of all, I express my gratefulness to Almighty God for successful completion of this research work.

I would like to express sincere gratitude to my supervisor Prof. Dr. A. K. M. Akther Hossain, Head, Department of Physics, BUET, for his guidance, valuable suggestions, encouragement, constructive criticism and inspiration in pursuing the whole investigation of the present research. Words are always insufficient to express his working capacities and unending enthusiasms for scientific rigorousness for innovative suggestions. This always becomes the everlasting source of inspiration for his students.

I would like to express my gratitude to Prof. Dr. Mominul Huq, Prof. Dr. Abu Hassan Bhuiyan, Prof. Dr. Jibon Podder, Prof. Dr. Firoz Alam Khan and Prof. Dr. Mostak Hossain, for their valuable suggestions through the study. It is my pleasure for me to extend my thanks to Associate Prof. Mrs. Fahima Khanam and Assistant Prof. Dr. Md. Farhad Mina and all other teachers of Physics Department for their cooperation.

I am grateful to Dr. Deba Prasad Paul, Professor, Department of Physics, University of Chittagong, for his valuable suggestions to prepare this thesis paper. I would like to thank my respected teachers Prof. Dr. Arun Kumar Deb, Prof. Dr. Mihir Kumar Roy and Prof. Dr. Md. Nurul Islam, Department of Physics, University of Chittagong, for their inspiration to complete my research work. I also thank my respected teacher Dr. A. K. M. Moinul Hoque Miaze, Associate Professor, Department of Physics, University of Chittagong for his valuable suggestions and providing necessary journals.

All staffs of Physics Department, BUET did extended help whenever I needed. I would like to thank them all.

Special thanks to Mr. Jasim Uddin Khan, Industrial Physics Division, BCSIR, Dhaka, for cooperation during permeability measurement.

I wish to thank specially my senior research workers Md. Farhad Alam, Md. Himidur Rahaman Khan, Mohammad Khurshed Alam and Tushar Shuvra Biswas. I am also thankfully acknowledging my friends Abdur Rahaman and Maruf for their inspiration and encouragement.

I am thankful to Ministry of Science and Information & Communication Technology, Government of the People's Republic of Bangladesh for granting the National Science and Information & Communication Technology (NSICT) for carrying out this work.

I would like to express my gratitude to my parents, brother and sister. This dissertation would never have been possible without their love and affections.

The Author
Sanjoy Kumar Nandi
Dhaka, August 2010

CONTENTS

CHAPTER 3

SAMPLE PREPARATION AND STRUCTURAL CHARACTERIZATION

CHAPTER 4

RESULTS AND DISCUSSION

CHAPTER-5
CONCLUSIONS

LIST OF FIGURES

LIST OF TABLES

LIST OF SYMBOLS AND ABBREVIATIONS

AC	Alternating current
B	Magnetic induction
d_1	Inner diameter of the toroid shaped sample
d_2	Outer diameter of the toroid shaped sample
d_{exp}	Experimental density
d_{th}	Theoretical density
H	Height of the sample
H	Magnetic field intensity
H_{cr}	Critical field
J	Exchange integral
K	Total anisotropy
K_1	Magnetocrystalline anisotropy
L_o	Inductance of the sample without winding
L_s	Inductance of the sample with winding
M	Magnetization
M_s	Saturation magnetization
N_A	Avogadroôs number
P	Porosity
P_{intra}	Intragonal porosity
P_{inter}	Intergonal porosity
Q	Relative quality factor
R	Resistive part of the complex impedance
T	Temperature
T_C	Curie temperature
T_N	Néel temperature
T_S	Sintering temperature
X	Reactive part of the complex impedance
Z	Complex impedance
ɤ	Angular velocity
ŭ	Phase lag
Ů	Permittivity
ɣ	Wave function
ε_i	Initial permeability
$\varepsilon_i^{/}$	Real part of initial permeability
$\varepsilon_i^{//}$	Complex part of initial permeability
ɢ	Susceptibility
$ɢ_{spin}$	Real part of complex susceptibility
$ɢ_w$	Complex part of complex susceptibility

CHAPTER-1
INTRODUCTION

1.1 Introduction

The ever-escalating use of equipments working in the micro- wave (MW) frequency range such as radar, wireless and mobile communication systems and home appliances has resulted in an increase in electromagnetic interference (EMI) as well as the intensity of this non-ionizing radiation [1ï 3]. This has resulted in an intensive research in the field of ôMW absorbing materialsô for their use in minimizing the harmful effect of electromagnetic (EM) waves on biological tissues as well as in the form of EMI, along with their so-called use as radar absorbing material (RAM) [3ï 6]. Among various types of MW absorbing materials that have been investigated, the magnetic material has been proven to be most functional due to the simultaneous presence of both dielectric and magnetic losses. Ferrite materials have been observed to exhibit substantial losses in the vicinity of ferromagnetic resonance (FMR) and dipole relaxation peak. The spinel ferrites can be used only up to 3 GHz frequency range, but the hexaferrites can be used in the whole GHz region, due to their intrinsic uni-axial anisotropic property. The hexaferrites are ferrites with complex crystal structure of AOï Fe_2O_3ï MeO (known as magneto-plumbite structure), where A=Ba, Sr, Ca, or La and M=a bivalent transition metal. The different stable phases of hexaferrite in the increasing order of complexity are M, Y, W, Z, X and U [4ï 6]. Structurally, all hexaferrite phases are made of by stacking a combination of R, S and T blocks directly or with inverted by180 degree. The skeleton of these blocks basically consists of different layers of oxygen in which some oxygen atom has been replaced by A (Ba, Sr, Ca, or La) atom. The metal and ferric ions occupy the interstitial (tetrahedral, octahedral and rhombohedral) sites in this frame. Among these stable phases, U-type hexaferrite phase that has the most complex crystal structure ($Ba_4Me_2Fe_{36}O_{60}$) and largest unit cell size has been least studied. Few reports regarding the procedure for preparation of single phase of U-type hexaferrite, its thermal stability range, crystal structure and observation of ferromagnetic resonance with cobalt as metallic ion had been reported [7ï 13].

In the present work, the preparation of Zn doped Ni_2U polycrystalline bulk samples was prepared by the conventional solid-state method. Complex permittivity and permeability were investigated in the frequency region of 50 Hzï 120 MHz. The effect of composition, annealing temperature and frequency on complex permeability and complex dielectric constants is investigated.

1.2 Objectives of the Present Work

Ferrites are especially convenient for high frequency uses because of their high resistivity. The high frequency response of the complex permeability is therefore very useful in determining the convenient frequency range in which a particular ferrite material can be used. The mechanism of eddy current losses and damping of domain wall motion can be understood from the relative magnitudes of the real and imaginary parts of the complex permeability. The effect of composition and microstructure on the frequency response is therefore very useful.

The main objectives of the present research are as follows:

- Preparation of various $Ba_4Ni_{2-x}Zn_xFe_{36}O_{60}$. (for x = 0.2, 0.4, 0.6, 0.8, 1.0, 1.2, compositions.
- Perform structural characterizations, density and porosity of the samples.
- Study of surface morphology (grain size).
- Initial permeability as a function of frequency (1 kHz-120MHz) for samples having various sintered temperature.

Possible outcome of the research is as follows:

Initial permeability and magnetization studies will reveal the influence of zinc doping on magnetic properties. The obtained permeability and magnetization will be helpful for the fabrication of permanent magnet, microwave devices and multilayer chip inductors (MLCIs).

1.3 Summary of the Thesis

The format of the thesis is as follows:

Chapter 1 of this thesis deals with the importance of hexaferrites and objectives of the present work.

Chapter 2 gives a brief overview of the materials, theoretical background as well as crystal structure of the spinel type ferrites.

Chapter 3 gives the details of the sample preparation and describes the descriptions of different measurements that have been used in this research work.

Chapter 4 is devoted to the results of various investigations of the study and explanation of results in the light of existing theories.

The conclusions drawn from the overall experimental results and discussion are presented in Chapter 5.

References

[1] Stonier, R. A., ñStealth aircraft and technology from World War II to the Gulf Part I. History and backgroundò, SAMPE J. 27, pp. 9ï 17(1991)

[2] Vittoria, C., ñFerrite uses at millimeter wavelengthò, J. Magn. Magn. Mater. Vol-21, No. 2, pp.109-118, (1980).

[3] Dishovski, N., Petkov, A., Nedkov, I. and Razkazov, I., ñHexaferrite contribution to microwave absorbers characteristicsò, IEEE Trans. Magn. Vol-30, No.2, pp. 969-971, (1994).

[4] Abbas, S. M., ñPreparation and characterization of microwave absorbing materialsò, Doctor Thesis, Indian Institute of Technology Delhi India, pp. 19ï 32,(2007).

[5] Smit, J., Wijn, H.P.J., ñFerrite: Physical Properties of Ferromagnetic Oxide in Relation to their Technical Applicationò, Philips Technical library, Netherland, pp. 176ï 210, (1959).

[6] Aulock, W.H.V., ñin: Hand book of Microwave Ferrite Materialsò, Academic Press, London, pp. 451ï 511, (1965).

[7] Lisjak, D., Bregar, V.B., Znidarsic, A., and Drofenik, M., ñMicrowave behavior of ferrite compositesò, J. Optoelectron. Adv. Mater. Vol- 8, No.1, pp.60-65, (2006).

[8] Lisjak, D. and Drofenik, M., ñThe thermal stability range and magnetic properties of U-type hexaferritesò, J. Magn. Magn. Mater. Vol-272-276, Supplement. 1, pp.1817-1819, (2004).

[9] Lisjak D. and Drofenik, M., ñSynthesis and characterization of Zn_2U: $Ba_4Zn_2Fe_{36}O_{60}$ hexaferrite powderò, J.Appl.Phys, Vol-93, No. 10, pp. 8011-8013, (2003).

[10] Sudakar, C., Subbanna G.N., and Kutty, T.R.N., ñWet chemical synthesis of multi-component hexaferrites by gel-to-crystallite conversion and their magnetic propertiesò, J. Magn. Magn. Mater. Vol-263, No. 3, pp. 253-268(2003).

[11] Lisjak, D., Macguiness P., and Drofenik, M., ñThermal instability of Co- substituted barium hexaferrites with U-type structureò, J. Mater. Res. Vol-21, No.2, pp. 420-427, (2006).

[12] Lisjak, D., Makovec D., and Drofenik, M., ñFormation of U-type hexaferritesò, J. Mater. Res. Vol-19, No.8, pp. 2462-2470, (2004).

[13] Haijun, Z., Zhichao, L., Xi, Y., Liangying, Z. and Mingzhong, W. ñComplex permeability and permittivity of $Ba_4Zn_{2-x}Co_xFe_{36}O_{60}$ U-type hexaferrites prepared by sol-gel on composition, annealing and frequencyò, Mat. Sci. Eng. B. Vol-97, No.2, pp. 160-166, (2003).

CHAPTER 2

LITERATURE REVIEW

Hexaferrites are important members of ferrimagnetic system commonly known as ferrites. The outstanding properties of ferrites are their complex magnetic structure, which can be varied to tailor their magnetic properties for various high frequency applications. In this chapter we describe a brief overview of the hexa ferrites. The basic issues of ferrimagnetism and crystal structure of the hexaferrites are discussed. A few theoretical aspects of complex permeability are also discussed.

2.1 Overview of the materials

In views of the chemistry inertia, interesting unique physical properties, and magnetic properties, hexagonal ferrite has potential applications as a high frequency microwave implements. Much attention has been focused on this group of materials over past 40 years [1-4]. The unit cell of the U-type compound formed by three molecules possesses the rhombohedral structure belonging to space group R3m. The structure is built up by the superposition of two M-blocks ($BaFe_{12}O_{19}$) and one Y-block ($Ba_2Me_2Fe_{12}O_{22}$) along the c-axis. Despite numerous studies of the hexaferrite family, knowledge of the so-called U hexaferrites is limited. However, only few works had been done on the magnetic properties of U-type hexaferrites. U-type hexaferrites are difficult to prepare in the single-phase condition due to their complex crystal structure [4]. Our aim was to investigate their temperature stability range and to optimize the preparation procedure using a solid-state reaction approach. For this reason some modifications to the classical approach were applied: high-energy milling instead of the usual wet milling and topotactic reaction [5].

Lisjak et al. [6] discussed the preparation of single phase polycrystalline $Ba_4Me_2Fe_{36}O_{60}$ ($Me = Co, Ni, Zn$), the stability range, and magnetic properties of U-type hexaferrites. U-hexaferrites are formed from the intermediate phases M-hexaferrite ($BaFe_{12}O_{19}$) and Y-hexaferrite ($Ba_2Me_2Fe_{12}O_{22}$), which at the same time represent units in the U-hexaferritesô crystal structure. The preparation of monophase U-hexaferrites was made by combining high-energy milling or chemical coprecipitation with a calcination at 1250ï 1300 °C [6-7]. Structural defects, such as stacking faults, were observed in monophase samples with a high-resolution transmission electron microscope. The observed defects can be

regarded as seeds for the formation of other hexaferrite phases after prolonged calcination times and higher calcination temperatures.

The reaction temperature requires for $Ba_4Co_2Fe_{36}O_{60}$ nanocrystals prepared through sol-gel method require were dramatically lower than that of conventional solid state reaction method [8]. The surface composition of the nanocrystalline $Ba_4Co_2Fe_{36}O_{60}$ was found to be different from that of the bulk counterpart material, exhibiting a higher content of Ba and Co. The magnetic properties of these samples were clearly size-dependent. The specific saturation magnetization was lower than that of bulk $Ba_4Co_2Fe_{36}O_{60}$ and decreases with the grain size.

Dimri et al. [9] studied magnetic and dielectric properties of bulk and thick film of Co_2U ($Ba_4Co_2Fe_{36}O_{60}$) prepared by the citrate method at radio and microwave frequencies. They observed that these thick films have lower values of dielectric and magnetic parameters both at low and microwave frequencies.

An early investigation measured the saturation magnetization parallel and perpendicular to c axis, anisotropy constant and field as a function from 4.2 to 600K [10]. Ferromagnetic resonance experiments were performed on Zn_2U ($Ba_4Zn_2Fe_{36}O_{60}$) and *Mn*-substituted Zn_2U single crystal spheres using a reflection technique and transverse pumping [11]. Effect of Zn substitution, annealing temperature and frequency on complex permeability and permittivity of $Ba_4Co_2Fe_{36}O_{60}$ has been reported by Haijun et al. [12]. This study showed the Zn substitution increase the permeability and permittivity and corresponding maximum values are obtained for the sample $Ba_4CoZnFe_{36}O_{60}$.

Complex permittivity, permeability and microwave absorbing properties of a U-type hexaferrite series $Ba_4Mn_{(2-x)}Zn_xFe_{36}O_{60}$ (with $0 \leq x < \leq$ in step of 0.5) have been examined in the X-band (8.2ï 12.4GHz) frequency range [15]. The series have been prepared using conventional solid state reaction route. Addition of Zn resulted in an increase in reflection loss from -4 dB (or 60% absorption) in sample with x= 0 to -32 dB (99.92% absorption) in sample with x=1 when the sample thickness was 1.7 mm. Multiple peaks of resonance were obtained in the dielectric and magnetic loss spectra and an increase of amplitude as well as width of dielectric and magnetic resonances observed for all samples. The result indicates that the sample with composition $Ba_4MnZnFe_{36}O_{60}$, i.e., x=1, can be used efectively for microwave absorption and suppression of electromagnetic interference.

2.2 Magnetic ordering

The onset of magnetic order in solids has two basic requirements:

(i) Individual atoms should have magnetic moments (spins),

(ii) Exchange interactions should exist that couple them together.

Magnetic moments originate in solids as a consequence of overlapping of the electronic wave function with those of neighboring atoms. This condition is best fulfilled by some transition metals and rare-earths. The exchange interactions depend sensitively upon the inter-atomic distance and the nature of the chemical bonds, particularly of nearest neighbour atoms. When the positive exchange dominates, which corresponds to parallel coupling of neighbouring atomic moments (spins), the magnetic system becomes ferromagnetic below a certain temperature T_C called the Curie temperature. The common spin directions are determined by the minimum of magneto-crystalline anisotropy energy of the crystal. Therefore, ferromagnetic substances are characterized by spontaneous magnetization. But a ferromagnetic material in the demagnetized state displays no net magnetization in zero field because in the demagnetized state a ferromagnetic of macroscopic size is divided into a number of small regions called domains, spontaneously magnetized to saturation value and the directions of these spontaneous magnetization of the various domains are such that the net magnetization of the specimen is zero. The existence of domains is a consequence of energy minimization. The size and formation of these domains is in a complicated manner dependent on the shape of the specimen as well as its magnetic and thermal history. When negative exchange dominates, adjacent atomic moments (spins) align antiparallel to each other, and the substance is said to be anti-ferromagnetic below a characteristic temperature, T_N, called the Néel temperature. In the simplest case, the lattice of an anti-ferromagnet is divided into two sublattices with the magnetic moments of these in anti-parallel alignment. This result is zero net magnetization. A special case of anti-ferromagnetism is ferrimagnetism. In ferrimagnetism, there are also two sublattices with magnetic moments in opposite directions, but the magnetization of the sublattices are of unequal strength resulting in a non-zero magnetization and therefore has net spontaneous magnetization. At the macroscopic level of domain structures, ferromagnetic and ferrimagnetic materials are therefore similar.

The Curie and Néel temperatures characterize a phase transition between the magnetically ordered and disordered (paramagnetic) states. From these simple cases of magnetic ordering various types of magnetic order exists, particularly in metallic substances. Because of long-range order and oscillatory nature of the exchange interaction, mediated by

the conduction electrons, structures like helical, conical and modulated patterns might occur. A useful property for characterizing the magnetic materials is the magnetic susceptibility, χ, defined as the magnetization, M, divided by the applied magnetic field, H i.e. $\chi = M / H$. The temperature dependence of susceptibility or, more accurately, inverse of susceptibility is a good characterization parameter for magnetic materials, Fig. 2.1. Fig. 2.1(e) shows that in the paramagnetic region, the variation of the inverse susceptibility with temperature of a ferrite material is decidedly non-linear. Thus the ferrite materials do not obey the Curie-Weiss law, $\chi = C/(T - T_C)$ [16].

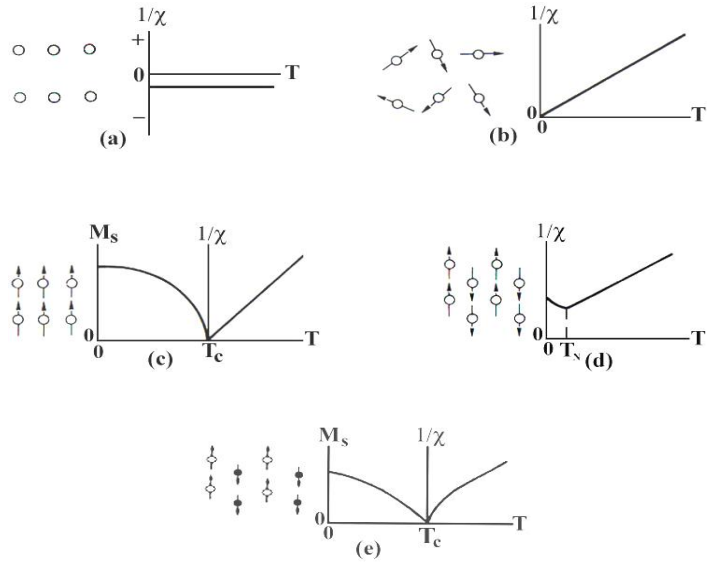

Fig. 2.1. Temperature dependence of the inverse susceptibility for: (a) a diamagnetic material; (b) a paramagnetic material, showing Curieôs law behaviour; (c) a ferromagnetic material, showing a spontaneous magnetization for $T<T_C$ and Curie-Weiss behaviour for $T>T_C$; (d) an antiferromagnetic material; (e) a ferrimagnetic material, showing a net spontaneous magnetization for $T<T_C$ and non linear behaviour for $T>T_C$.

2.3 Hexaferrites

The hexaferrites are ferrites with complex crystal structure of AOï Fe_2O_3ï MeO (known as magneto-plumbite structure), where A=Ba, Sr, Ca, or La and Me=a bivalent transition metal These are classified into five main types depending on their chemical formulas and crystal

structure: the M-type ($BaFe_{12}O_{19}$), W-type ($BaMe_2Fe_{16}O_{27}$), X-type ($BaMe_2Fe_{28}O_{46}$), Y-type ($Ba_2Me_2Fe_{12}O_{22}$), Z-type ($Ba_2Me_2Fe_{24}O_{41}$) and U-type $Ba_4Me_2Fe_{36}O_{60}$ [16-19]. Structurally, all hexaferrite phases are made of by stacking a combination of R, S and T blocks directly or with inverted by180^0. As shown in Table 1, the structures of M-type, W-type, Y-type and Z-type ferrites depend on the combination of layers, where R and T layers contain Ba^{+2}, Sr^{+2} or Pb^{+2} ions [18]. The S unit is formed by two formula units $MeFe_2O_4$ with spinal structure thus containing two tetrahedral and four octahedral cation sites. The R block has the stoichiometry $(BaFe_60_{11})^{2-}$, with three octahedral sites of two different types and one bypyramidal, five-fold cation site; the Ba^{2+} occupies an O^2 ,12-fold site, Fig. 2.1. The T unit has four layers with formula $Ba_2 F_{38}O_{14}$, where the Fe ions occupy the two octahedral sites, and six octahedral sites of two different types. The block lengths are 4.4.81, 11.61 and 14.52 for the S and SR and TS blocks respectively [19]. Star (*) over a block represents the 180^0 rotation of the corresponding block about the c axis. The R and T block are shown in Fig. 2.2. The table

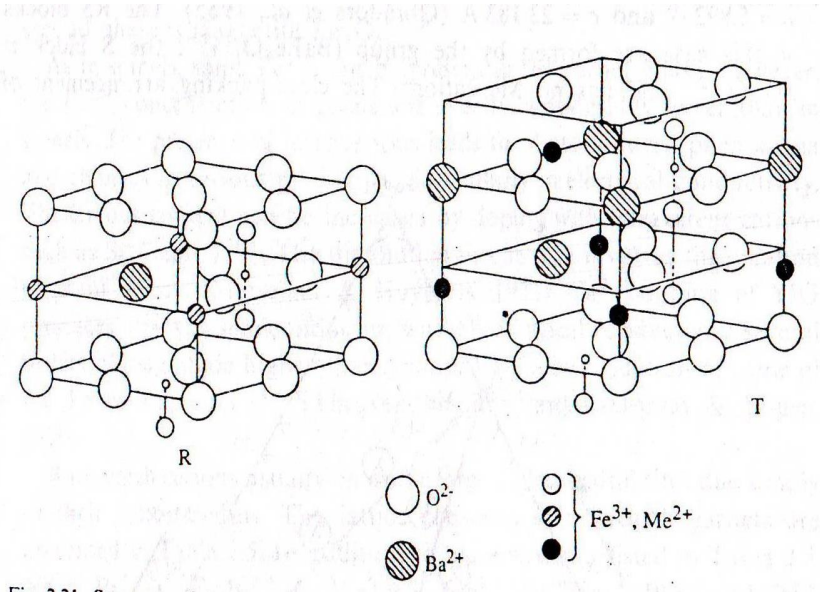

Fig.2.2. Structure of the R and T block units in hexagonal ferrites

Table. 2.1: Building block and formulae of hexagonal ferrites

Designation	Formula	Building block	No. of Molecules per unit cell
M	$BaFe_{12}O_{19}$	RSR*S*	2
Y	$Ba_2Me_2Fe_{12}O_{22}$	$(TS)_3$	3
W	$BaMe_2Fe_{16}O_{27}$	$R(S)_2R^*(S^*)_2$	2
X	$BaMe_2Fe_{28}O_{46}$	$(RSR^*S^*_2)_3$	2
Z	$Ba_2Me_2Fe_{24}O_{41}$	RSTSR*S*T*S*	2
U	$Ba_4Me_2Fe_{36}O_{60}$	RSR*S*T*S*	3

2.4 U-type hexaferrites

Two types of hexaferrites can be distinguished in terms of crystal structure: M_mS_n and M_mY_n, which are composed of M and S, and M and Y blocks, respectively. In Table I the most well-known types of hexaferrites and those with the biggest unit cells are listed. Hexaferrites of the M_mY_n type greatly outnumber those of the M_mS_n type [20-21]. U-type hexaferrites with the composition $Ba_4Me_2Fe_{36}O_{60}$ are of the M_mY_n type, i.e., M_2Y. Using the same description as for the M- and Y-hexaferritesô crystal structure, that of the U-hexaferrites can be described as

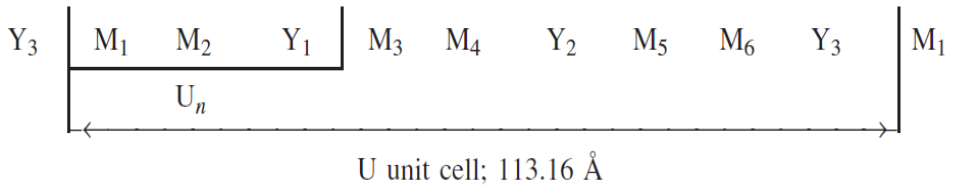

Fig.2.3. U-type hexaferritesô crystal structure

Three different combinations of M_2Y blocks form a triple hexagonal unit cell of U-hexaferrites with a =5.88 Å and c = 113.2 Å. The same unit-cell parameters and the rhombohedral space group R3m were determined for the $Ba_4Zn_2Fe_{36}O_{60}$ monocrystal by Kerecman et al.[13].The structure of M-type and Y-type hexaferrites are shown in Fig. 2.4. On the basis of this structure cation distribution of U-type hexaferrites is given is Table 2.2.

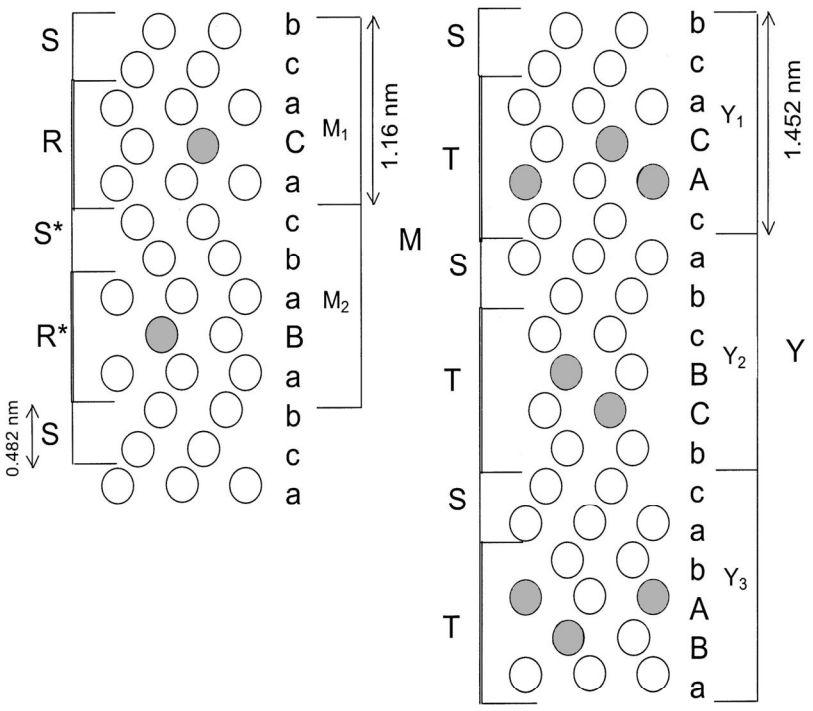

Fig.2.4. M- and Y-hexaferritesô crystal structure

Table 2.2: Cation distribution in U-type hexaferrite

Sublattice	**Coordination**	**Block**	**No of ions per unit cell**	**Spin**
C_{IV}	tetrahedral	S	6	Down
a_{VI}	Octahedral	S	3	Up
h_{VI}	Octahedral	T-S	18	Up
c_{VI}	Octahedral	T	6	Down
c_{VI}	Tetrahedral	T	6	Down
b_{VI}	Octahedral	T	3	Up
K	Octahedral	R-S	36	Up
f_{VI}	Octahedral	R	12	Up
A	Octahedral	S	6	Up
f_{IV}	Tetrahedral	S	12	Down
B	Five-fold	R	6	Up

2.5. Exchange interactions in ferrites

The intense short-range electrostatic field, which is responsible for the magnetic ordering, is the exchange force that is quantum mechanical in origin and is related to the overlapping of total wave functions of the neighbouring atoms. The total wave function consists of the orbital and spin motions. Usually the net quantum number is written as S, because the magnetic moments arise mostly due to the spin motion as described above. The exchange interactions coupling the spins of a pair of electrons are proportional to the scalar product of their spin vectors [22-24],

$$V_{ij} = -2J_{ij}\vec{S}_{i.}.\vec{S}_{j} \tag{2.1}$$

where J_{ij} is the exchange integral given in a self explanatory notation by

$$J_{ij} = \int \psi_i^*(1)\psi_j^*(2)\left[\frac{1}{r_{12}} + \frac{1}{r_{ij}} - \frac{1}{r_{i1}} - \frac{1}{r_{j2}}\right]\psi_i(2)\psi_j(2)dv_1 dv_2 \tag{2.2}$$

In this expression r ôs are the distances, subscripts i and j refer to the atoms, 1 and 2 refers to the two electrons. If the J in equation (2.1) is positive, we achieve ferromagnetism. A negative J may give rise to anti-ferromagnetism or ferrimagnetism.

Magnetic interactions in ferrites as well as in some ionic compounds are different from the one considered above because the cations are mutually separated by bigger anions (oxygen ions). These anions obscure the direct overlapping of the cation charge distributions, sometimes partially and some times completely making the direct exchange interaction very weak. Cations are too far apart in most oxides for a direct cation-cation interaction. Instead, superexchange interactions appear, i.e., indirect exchange via anion p-orbitals that may be strong enough to order the magnetic moments. Apart from the electronic structure of cations this type of interactions strongly depends on the geometry of arrangement of the two interacting cations and the intervening anion. Both the distance and the angles are relevant. Usually only the interactions with in first coordination sphere (when both the cations are in contact with the anion) are important. In the Neél theory of ferrimagnetism the interactions taken as effective are inter- and intra-sublattice interactions A-B, A-A and B-B. The type of magnetic order depends on their relative strength.

The superexchange mechanism between cations that operate via the intermediate anions was proposed by Kramer for such cases and was developed by Anderson and Van Vleck [23]. A simple example of superexchange is provided by MnO which was chosen by Anderson. From the crystal structure of MnO it will be seen that the antiparallel manganese ions are collinear with their neighbouring oxygen ions. The O^{2-} ions each have six 2p electrons in three antiparallel pairs. The outer electrons of the Mn^{2+} ions are in 3d sub-shells which are

half filled with five electrons in each. The phenomenon of superexchange is considered to be due to an overlap between the manganese 3d orbits and the oxygen 2p orbits with a continuous interchange of electrons between them. It appears that, for the overall energy of the system to be a minimum, the moments of the manganese ions on either side of the oxygen ion must be antiparallel. The manganese magnetic moments are thus, in effect, coupled through the intervening oxygen ion. The idea is illustrated in Fig. 2.5.

In Figs. 2.5(a) and 2.5(c) the outer electrons in a pair of Mn^{2+} ions, and in an intervening O^{2-} ion in the unexcited state, are shown by the arrows. One suggested mode of coupling is indicated in Fig. 2.5(b). The two electrons of a pair in the oxygen ion are simultaneously transferred, one to the left and the other to the right. If their directions of spin are unchanged then, by Hundôs rules, the moments of the two manganese ions must be antiparallel as shown. Another possibility is represented in Fig. 2.5(d). One electron only has been transferred to the manganese ion on the left. The oxygen ion now has a moment of $1\mu_B$ and if there is negative interaction between the oxygen ion and the right-hand manganese ion then again the moments of the manganese ions will be antiparallel. If these ideas are accepted then the oxygen ions play an essential part in producing antiferromagnetism in the oxide. Moreover, because of the dumbbell shape of the 2p orbits, the coupling mechanism should be most effective when the metal ions and the oxygen ions lie in one straight line, that is, the angle between the bonds is 180°, and this is the case with MnO.

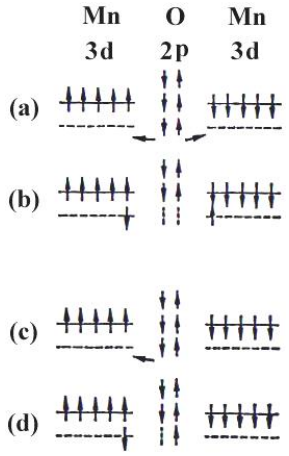

Fig. 2.5. Illustrating superexchange in MnO

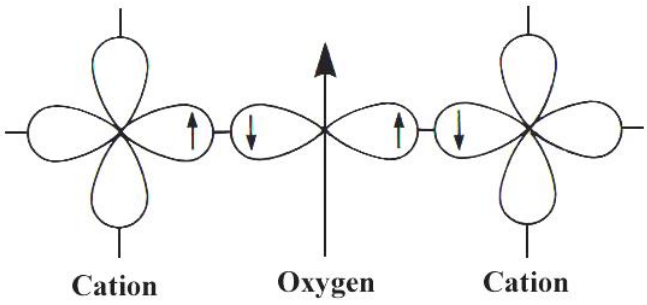

Fig. 2.6. Schematic representation of the superexchange interaction in the magnetic oxides. The p orbital of an anion (center) interact with the d orbitals of the transitional metal cations.

In the case of ferrites the coupling is of the indirect type which involves overlapping of oxygen wave functions with those of the neighboring cations. Consider two transition metal cations separated by an O, Fig. 2.6. The O^{2-} has no net magnetic moment since it has completely filled shells, with p-type outermost orbitals. Orbital p_x has two electrons: one with spin up, and the other with spin down, consistent with pauliôs exclusion principle. The essential point is that when an oxygen p orbital overlaps with a cation d orbital, one of the p electrons can be accepted by the cations. When one of the transition-metal cations is brought close the O^{2-}, partial electron overlap (between a 3d electron from the cation and a 2p electron form the O^{2-}) can occur only for antiparallel spins, because electrons with the same spin are repelled. Empty 3d states in the cation are available for partial occupation by the O^{2-} electron, with an antiparallel orientation. Electron overlap between the other cation and the O^{2-} then occurs resulting in antiparallel spins and therefore antiparallel order between the cations. Since the p orbitals are linear, the strongest interaction is expected to take place for cation–O^{2-}–cation angles close to 180^0 [25].

2.5.2. Néel theory of ferrimagnetism

If we consider the simplest case of a two-sublattice system having antiparallel and non-equal magnetic moments, the inequality may be due to:

1) different elements in different sites,

2) same element in different ionic states, and
3) different crystalline fields leading to different effective moments for ions having the same spin.

The spins on one sublattice are under the influence of exchange forces due to the spins on the second sublattice as well as due to other spins on the same sublattice. The molecular fields acting on the two sublattices A and B can be written as [23,25-26]

$$\vec{H}_A = \lambda_{AA}\vec{M}_A + \lambda_{AB}\vec{M}_B ,$$

$$\vec{H}_B = \lambda_{AB}\vec{M}_A + \lambda_{BB}\vec{M}_B$$

where $\vec{M}_A$ and $\vec{M}_B$ are the magnetizations of the two sublattices and λ's are the Weiss constants. Since the interaction between the sublattices is antiferromagnetic, λ_{AB} must be negative, but λ_{AA} and λ_{BB} may be negative or positive depending on the crystal structure and the nature of the interacting atoms. Probably, these interactions are also negative, though they are in general quite small.

Assuming all the exchange interactions to be negative the molecular fields will be then given by

$$.\vec{H}_A = -\lambda_{AA}\vec{M}_A - \lambda_{AB}\vec{M}_B ,$$

$$\vec{H}_B = -\lambda_{AB}\vec{M}_A - \lambda_{BB}\vec{M}_B$$

Since in general, λ_{AA} and λ_{BB} are small compared to λ_{AB}, it is convenient to express the strengths of these interactions relative to the dominant λ_{AB} interaction.

Let $\lambda_{AA} = \alpha\lambda_{AB}$

and $\lambda_{BB} = \beta\lambda_{AB}$

In an external applied field $\vec{H}$, the fields acting on A and B sites are

$$\vec{H}_A = \vec{H} - \lambda_{AB}(\alpha\vec{M}_A - \vec{M}_B) ,$$

$$\vec{H}_B = \vec{H} - \lambda_{AB}(\vec{M}_A - \beta\vec{M}_B)$$

At temperatures higher than the transition temperature, T_N, $\vec{H}_A$, $\vec{M}_A$ and $\vec{M}_B$ are all parallel and we can write

$$\vec{M}_A = \frac{C_A}{T}[\vec{H} - \lambda_{AB}(\alpha\vec{M}_A - \vec{M}_B)], \qquad (2.3)$$

$$\vec{M}_B = \frac{C_B}{T}[\vec{H} - \lambda_{AB}(\vec{M}_A - \beta\vec{M}_B)] \tag{2.4}$$

where C_A and C_B are the Curie constants for the two sublattices.

$$C_A = N_A g\mu_B^2 S_A(S_A+1)/3K$$

and $$C_B = N_B g\mu_B^2 S_B(S_B+1)/3K$$

N_A and N_B denote the number of magnetic ions on A and B sites respectively and S_A and S_B are their spin quantum numbers. Solving for the susceptibility, χ, one gets [25,26]

$$\frac{1}{\chi} = \frac{T}{C} - \frac{1}{\chi_0} - \frac{b}{T-\theta}$$

$$\frac{1}{\chi} = \frac{T + (C/\chi_0)}{C} - \frac{b}{T-\theta} \tag{2.5}$$

where C, χ_0, b and θ are constants for particular substance and are given by

$$C = C_A + C_B$$

$$\frac{1}{\chi_0} = -\frac{1}{C^2}[C_A^2\lambda_{AA} + C_B^2\lambda_{BB} + 2C_AC_B\lambda_{AB}]$$

$$b = \frac{C_AC_B}{C^3}[C_A^2(\lambda_{AA}-\lambda_{BB})^2 + C_B^2(\lambda_{BB}-\lambda_{AB})^2 - 2C_AC_B\{\lambda_{AB}^2 - (\lambda_{AA}+\lambda_{BB})\lambda_{AB} + \lambda_{AA}\lambda_{BB}\}]$$

$$\theta = -\frac{C_AC_B}{C}(\lambda_{AB}+\lambda_{BB}) - 2\lambda_{AB}$$

Equation (2.5) represents a hyperbola, and the physically meaning part of it is plotted in Fig. 2.7. This curvature of the plot of 1/χ versus T is a characteristics feature of a ferrimagnet. It cuts the temperature axis at T_C, called the Ferrimagnetic Curie point. At high temperatures the last term of equation (2.5) become negligible, and reduces to a Curie-Weiss law:

$$\chi = \frac{C}{T + (C/\chi_0)}$$

This is the equation of straight line, shown dashed in Fig. 2.7, to which the 1/χ versus T curve becomes asymptotic at high temperatures.

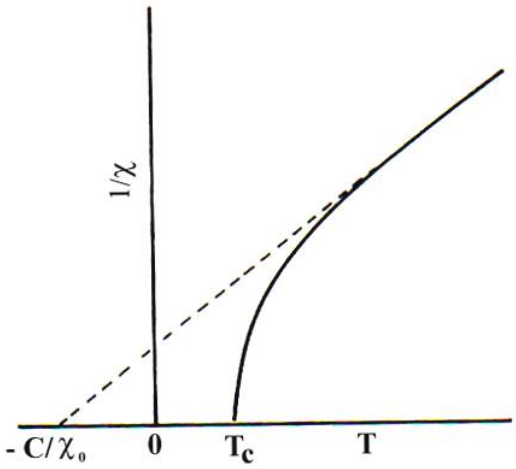

Fig. 2.7. The temperature dependence of the inverse susceptibility for ferrimagnets

The Ferrimagnetic Curie temperature T_C is obtained from equations (2.3) and (2.4) with $H = 0$ and setting the determinant of the coefficients of M_i equal to zero. This gives

$$T_C = \frac{1}{2}[C_A\lambda_{AA} + C_B\lambda_{BB} + \{(C_A\lambda_{AA} - C_B\lambda_{BB})^2 + 4C_AC_B\lambda_{AB}^2\}^2] \qquad (2.6)$$

Equation (2.5) is in good agreement with the experiment, except near the Curie point. The experimental Curie temperature, the temperature at which the susceptibility becomes infinite and spontaneous magnetization appears, is lower than the theoretical Curie temperature [26]. This disagreement between theory and experiment in the region of Curie point is presumably due to the short-range spin order (spin clusters) at temperatures above experimental T_C [25, 26].

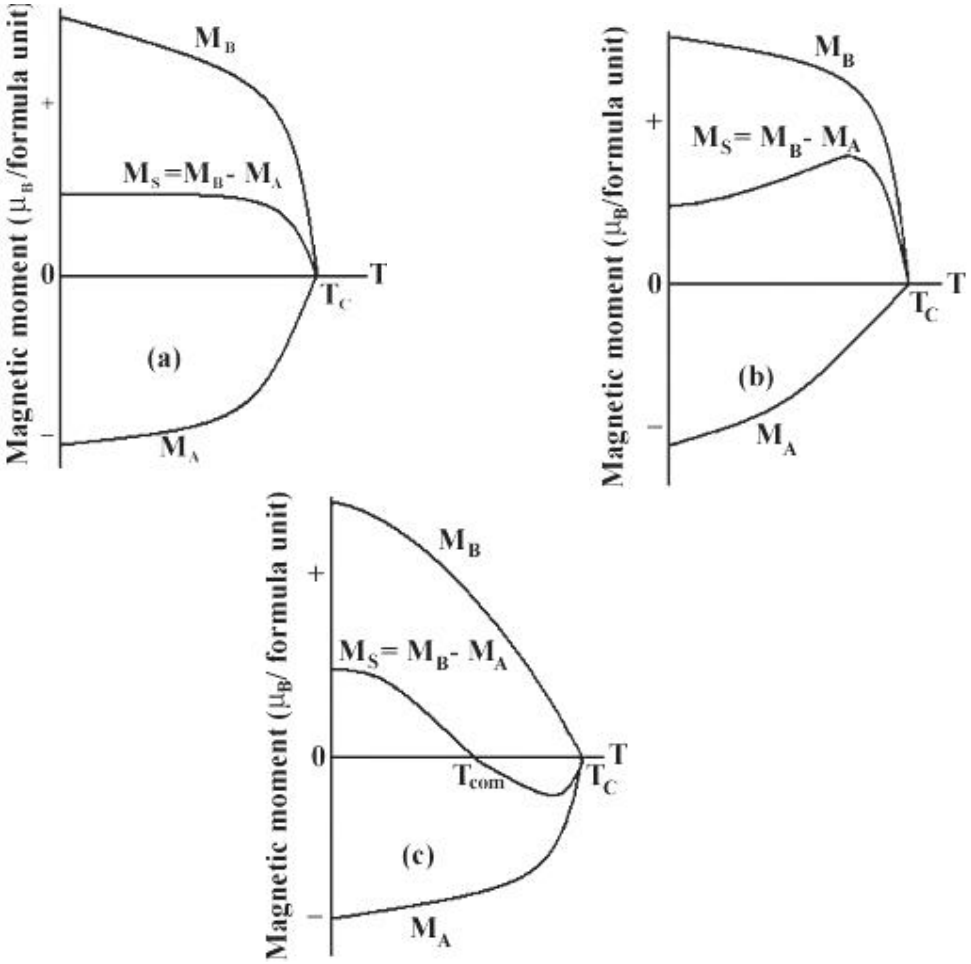

Fig. 2.8. Superposition of various combinations of two opposing sublattice magnetizations producing differing resultants including one with a compensation point (schematic)

The sublattice magnetizations will in general have different temperature dependences because the effective molecular fields acting on them are different. This suggests the possibility of having anomaly in the net magnetization versus temperature curves, Fig. 2.8. For most ferrimagnets the curve is similar to that of ferromagnets, but in a few cases there be a compensation point in the curve, Fig. 2.8(c) [27, 28]. At a point below the Curie temperature point, the two sublattice magnetizations are equal and thus appear to have no moment. This temperature is called the compensation point. Below this temperature one sublattice magnetization is larger

and provides the net moment. Above this temperature the other magnetization does dominates and the net magnetization reverses direction.

The essential requisite for Néel configuration is a strong negative exchange interaction between A and B sublattices which results in their being magnetized in opposite directions below the transition point. But there may be cases where intrasublattice interactions are comparable with intersublattice interaction. Neel's theory predicts paramagnetism for such substances at all temperatures. This is unreasonable since strong AA or BB interaction may lead to some kind of ordering especially at low temperature. In the cases of no AB interaction, antiferromagnetic ordering may be expected either in the A or in the B sublattice. Under certain conditions there may be non-collinear spin arrays of still lower energy.

2.7 Microstructure

A polycrystal is much more than many tiny crystals bonded together. The interfaces between the crystals, or the grain boundaries which separate and bond the grains, are complex and interactive interfaces. The whole set of a given materialôs properties (mechanical, chemical and especially electrical and magnetic) depend strongly on the nature of the microstructure.

In the simplest case, the grain boundary is the region, which accommodates the difference in crystallographic orientation between the neighbouring grains. For certain simple arrangements, the grain boundary is made of an array of dislocations whose number and spacing depends on the angular deviation between the grains. The ionic nature of ferrites leads to dislocation patterns considerably more complex than in metals, since electrostatic energy accounts for a significant fraction of the total boundary energy [25].

For low-loss ferrite, Ghate [27] states that the grain boundaries influence properties by

1) creating a high ressistivity intergranular layer,
2) acting as a sink for impurities which may act as a sintering aid and grain growth modifiers,
3) providing a path for oxygen diffusion, which may modify the oxidation state of cations near the boundaries.

In addition to grain boundaries, ceramic imperfections can impede domain wall motion and thus reduce the magnetic property. Among these are pores, cracks, inclusions, second phases, as well as residual strains. Imperfections also act as energy wells that pin the domain walls and require higher activation energy to detach. Stresses are microstructural imperfections that can result from impurities or processing problems such as too rapid a cool. They affect the domain dynamics and are responsible for a much greater share of the degradation of properties than would expect [27].

Grain growth kinetics depends strongly on the impurity content. A minor dopant can drastically change the nature and concentration of defects in the matrix, affecting grain boundary motion, pore mobility and pore removal [25, 29]. The effect of a given dopant depends on its valence and solubility with respect to host material. If it is not soluble at the sintering temperature, the dopant becomes a second phase which usually segregates to the grain boundary.

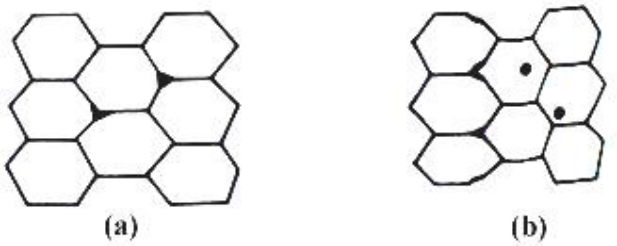

Fig. 2.9. Porosity character: (a) intergranular, (b) intragranular.

The porosity of ceramic samples results from two sources, intragranular porosity and intergranular porosity, Fig. 2.9. An undesirable effect in ceramic samples is the formation of exaggerated or discontinuous grain growth which is characterized by the excessive growth of some grains at the expense of small, neighbouring ones, Fig. 2.10. When this occurs, the large grain has a high defect concentration. Discontinuous growth is believed to result from one or several of the following: powder mixtures with impurities; a very large distribution of initial particle size; sintering at excessively high temperatures; in ferrites containing Zn and /or Mn, a low O_2 partial pressure in the sintering atmosphere. When a very large grain is surrounded by smaller ones, it is called ódouplexô microstructure.

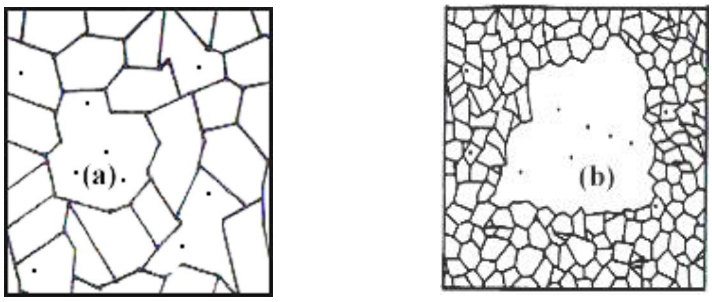

Fig. 2.10. Grain growth (a) discontinuous, (b) duplex (schematic)

2.8 Theories of permeability

Permeability is defined as the proportionality constant between the magnetic field induction B and applied field intensity H [25,26,30]:

$$B = \mu H \tag{2.7}$$

If the applied field is very low, approaching zero, the ratio will be called the initial permeability, Fig. 2.11 and is given by

$$\mu_i = \frac{\Delta B}{\Delta H}_{(\Delta H \to 0)}$$

This simple definition needs further sophistications. A magnetic material subjected to an ac magnetic field can be written as

$$H = H_0 e^{i\omega t} \tag{2.8}$$

It is observed that the magnetic flux density B lag behind H. This is caused due to the presence of various losses and is thus expressed as

$$B = B_0 e^{i(\omega t-\delta)} \tag{2.9}$$

Here δ is the phase angle that marks the delay of B with respect to H. The permeability is then given by

$$\mu = \frac{B}{H} = \frac{B_0 e^{i(\omega t-\delta)}}{H_0 e^{i\omega t}} = \frac{B_0 e^{-i\delta}}{H_0} = \frac{B_0}{H_0}\cos\delta - i\frac{B_0}{H_0}\sin\delta = \mu^{/} - i\mu^{//} \tag{2.10}$$

where $$\mu^{/} = \frac{B_0}{H_0}\cos\delta \tag{2.11}$$

and $$\mu'' = \frac{B_0}{H_0}\sin\delta \tag{2.12}$$

The real part (μ') of complex permeability (μ), as expressed in equation (2.10) represents the component of B which is in phase with H, so it corresponds to the normal permeability. If there are no losses, we should have $\mu = \mu'$. The imaginary part μ'' corresponds to that of B, which is delayed by phase angle 90^0 from H [16,24]. The presence of such a component requires a supply of energy to maintain the alternating magnetization, regardless of the origin of delay. The ratio of μ'' to μ', as is evident from equation (2.12) and (2.11) gives

$$\frac{\mu''}{\mu'} = \frac{\frac{B_0}{H_0}\sin\delta}{\frac{B_0}{H_0}\cos\delta} = \tan\delta \tag{2.13}$$

This $\tan\delta$ is called loss factor.

The quality factor is defined as the reciprocal of this loss factor, i.e.

$$\text{Quality factor} = \frac{1}{\tan\delta} \tag{2.14}$$

And the relative quality factor, $Q = \frac{\mu'}{\tan\delta}$ (2.15)

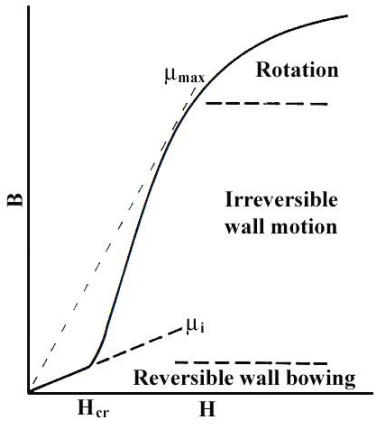

Fig. 2.11. Schematic magnetization curve showing the important parameter: initial permeability, μ_i (the slope of the curve at low fields) and the main magnetization mechanism in each magnetization range.

The curves that show the variation of both μ' and μ'' with frequency are called the magnetic spectrum or permeability spectrum of the material [16]. The variation of permeability with frequency is referred to as dispersion. The measurement of complex permeability gives us valuable information about the nature of domain wall and their movements. In dynamic measurements the eddy current loss is very important. This occurs due to the irreversible domain wall movements. The permeability of a ferrimagnetic substance is the combined effect of the wall permeability and rotational permeability mechanisms.

2.8.1 Mechanisms of permeability

The mechanisms can be explained as follows: A demagnetized magnetic material is divided into number of Weiss domains separated by Bloch walls. In each domain all the magnetic moments are oriented in parallel and the magnetization has its saturation value M_s. In the walls the magnetization direction changes gradually from the direction of magnetization in one domain to that in the next. The equilibrium positions of the walls result from the interactions with the magnetization in neighboring domains and from the influence of pores; crystal boundaries and chemical inhomogeneities which tend to favour certain wall positions.

2.8.1.1 Wall Permeability

The mechanism of wall permeability arises from the displacement of the domain walls in small fields. Lets us consider a piece of material in the demagnetized state, divided into Weiss domains with equal thickness L by means of 180° Bloch walls (as in the Fig. 2.12). The walls are parallel to the YZ plane. The magnetization M_s in the domains is oriented alternately in the $+Z$ or $-Z$ direction. When a field H with a component in the $+Z$ direction is applied, the magnetization in this direction will be favoured. A displacement dx of the walls in the direction shown by the dotted lines will decrease the energy density by an amount [31-32]:

$$\frac{2M_s H_z dx}{L}$$

This can be described as a pressure $M_s H_z$ exerted on each wall. The pressure will be counteracted by restoring forces which for small deviations may assume to be kdx per unit wall surface. The new equilibrium position is then given by

$$d = \frac{M_s H_z dx}{L}$$

From the change in the magnetization

$$\Delta M = \frac{2M_s d}{L},$$

the wall susceptibility χ_w may be calculated. Let H makes the angle θ with Z direction. The magnetization in the θ direction becomes

$$(\Delta M)_\theta = \frac{2M_s d}{L}\cos\theta, \text{ And with } H_z = H\cos\theta \text{ and } d = \frac{2M_s H_z}{K}$$

we obtain

$$\chi_w = \frac{(\Delta M)_\theta}{H} = \frac{4M_s^2 \cos^2\theta}{KL} \qquad (2.16)$$

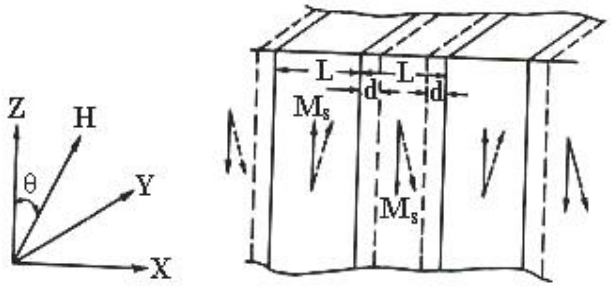

Fig. 2.12. Magnetization by wall motion and spin rotation.

2.8.1.2 Rotational Permeability

The rotational permeability mechanism arises from rotation of the magnetization in each domain. The direction of M can be found by minimizing the magnetic energy E as a function of the orientation. Major contribution to E comes from the crystal anisotropy energy. Other contributions may be due to the stress and shape anisotropy. The stress may influence the magnetic energy via the magnetostriction. The shape anisotropy

is caused by the boundaries of the sample as well as by pores, nonmagnetic inclusions and inhomogeneities. For small angular deviations, α_x and α_y may be written as

$$\alpha_x = \frac{M_x}{M_s} \text{ and } \alpha_y = \frac{M_y}{M_s}.$$

For equilibrium Z-direction, E may be expressed as [24, 25]

$$E = E_0 + \frac{1}{2}\alpha_x^2 E_{xx} + \frac{1}{2}\alpha_y^2 E_{yy}$$

where it is assumed that x and y are the principal axes of the energy minimum. Instead of E_{xx} & E_{yy}, the anisotropy field H_x^A and H_y^A are often introduced. Their magnitude is given by

$$H_x^A = \frac{E_{xx}}{2M_s} \text{ and } H_y^A = \frac{E_{yy}}{2M_s},$$

H_x^A & H_y^A represent the stiffness with which the magnetization is bound to the equilibrium direction for deviations in the x and y direction, respectively. The rotational susceptibilities $\chi_{r,x}$ and $\chi_{r,y}$ for fields applied along x and y directions, respectively are

$$\chi_{r,x} = \frac{M_s}{H_x^A} \text{ and } \chi_{r,y} = \frac{M_s}{H_y^A}.$$

For cubic materials it is often found that H_x^A and H_y^A are equal. For $H_x^A = H_y^A = H^A$ and a field H which makes an angle θ with the Z direction (as shown in Fig. 2.12) the rotational susceptibility, $\chi_{r,c}$ in one crystallite becomes

$$\chi_{r,c} = \frac{M_s}{H^A}\sin^2\theta \qquad (2.17)$$

A polycrystalline material consisting of a large number of randomly oriented grains of different shapes, with each grain divided into domains in a certain way. The rotational susceptibility χ_r of the material has to be obtained as a weighted average of $\chi_{r,c}$ of each crystallite, where the mutual influence of neighbouring crystallites has to be taken into account. If the crystal anisotropy dominates other anisotropies, then H^A will be constant throughout the material, so only the factor $\sin^2\theta$ (equation 2.17) has to be averaged. Snoek [28] assuming a linear averaging of $\chi_{r,c}$ and found

$$\chi_r = \frac{2M_s}{3H^A}$$

The total internal susceptibility

$$\chi = \chi_w + \chi_r = \frac{4M_s^2 \cos^2 \theta}{KL} + \frac{2M_s}{3H^A} \tag{2.18}$$

If the shape and stress anisotropies cannot be neglected, H^A will be larger. Any estimate of χ_r will then be rather uncertain as long as the domain structure, and the pore distribution in the material are not known. A similar estimate of χ_w would require knowledge of the stiffness parameter k and the domain width L. These parameters are influenced by such factors as imperfection, porosity and crystallite shape and distribution which are essentially unknown.

References

[1] Puliar, RC., Appleton, S.G., and Bhattacharya, A.K., ñThe Microwave Properties of Aligned Hexagonal Ferrite Fibersò, J. Mat. Sci. Lett. Vol-17, pp. 973-975, (1998).

[2] Kown, H.J. Shin J.Y., and Oh, J.H., ñThe microwave absorbing and resonance $Ba_3Co_{1.3}Zn_{0.3}Cu_{0.4}Fe_{24}O_{41}$hexagonal ferrite microwave absorbersò, J. Appl. Phys. Vol- 75, No. 10, pp.6109-6111,(1994).

[3] Sankaranarayanan, K., Pankhurst, Q.A., Dickson, D.P.E. and Johnson, C.E., ñUltrafine particles of barium ferrite from a citrate precursorò, J.Magn. Mag. Mat. Vol-120, No.1-3, pp.73-75, (1993).

[4] Tauber, A., Medill, J.S., and Shappirio, J.R., ñMagnetic Properties of $Ba_2Zn_2Fe_{28}O_{46}$ and $Ba_2Co_2Fe_{28}O_{46}$ Single Crystalsò, J. Appl. Phys. Vol-41, 1353-1354, (1970).

[5] Haijun, Z., Zhichao, L., Chengliang, M., Xi, Y., Liangying, Z., and Mingzhong, W., ñComplex permittivity, permeability, and microwave absorption of Zn- and Ti-substituted barium ferrite by citrate sol-gel processò, Mater. Sci. Eng. B, Vol-96, No. 3, pp.289-295, (2002).

[6] Wijn, H.P.J.,ñHexagonal ferrites,ò in Landolt-Börnstein Numerical Data and Functional Relationships in Science and Technology New Series, K.-H. Hellwege, Ed. New York: Spinger, pt. b, Vol-4, ch. 7, pp. 558. Group III, (1970).

[7] Winkler, G., ñReactivity of Solidsò, Elsevier publishing Co., New York, pp.189, (1965).

[8] Lisjak D. and Drofenik, M. ñThe thermal stability range and magnetic properties of U-type hexaferrites,ò J. Magn. Magn. Mater., Vol-272-276, Supliment-1, pp.1817-1819, (2004).

[9] Lisjak, D., Makovec, D. and Drofenik, M., ñFormation of U-type hexaferritesò, J. Mater. Res., Vo-19, No.8, pp.2464-2469, (2004).

[10] Xion, G., Xu, M. and Mai, Z. Magnetic proerties of $Ba_4Co_2Fe_{36}O_{60}$ nanocrystals prepared through a sol-gel method, Solid State Communications, Vol-118, No. 1, pp.53-58, (2001).

[11] Dimri, M.C., S.C. Kashyap, S.C. and Dube, D.C. ñComplex Permitivity and permeability of Co_2U ($Ba_4Co_2Fe_{36}O_{60}$) hexaferrites bulk and composite thick films at adio and microwave frequenciesò, IEEE transactions on Magnets, Vol-42 No.11, pp.3635-3640, (2006).

[12] Kerecman, A.J., Tauber, A., AuCoin, T.R. and Savage,R.O., ñMagnetic Properties of $Ba_4Zn_2Fe_{36}O_{60}$ò, Single Crystals J. Appl. Phys. Vol-39 No. 2, pp.726-726 (1968).

[13] Kerecman, A.J., Aucoin T.R., and Dattilo, W.P., ñFerromagnetic Resonance in $Ba_4Zn_2Fe_{36}O_{60}$ (Zn_2U) and Mn -Substituted Zn_2U Single Crystalsò, J. of Appl. Phys. Vol-40 No. 3, pp. 1416-1417, (1969).

[14] Haijun, Z., Zhichao, L., Xi, Y., Liangying Z., and Mingzhong, W. ñcomplex permeability and permittivity of $Ba_4Zn_{2-x}Co_xFe_{36}O_{60}$ U-type hexaferrites prepared by sol-gel on composition, annealing and frequencyò, Mat. Sci. Eng. B. Vol-97, No. 2, pp.160-166, (2003).

[15] Meena, R.S., Bhattachrya, S. and Chatterjee, R., ñComplex permittivity, permeability and microwave absorbing properties of ($Mn_{2-x}Zn_x$)U-type hexaferriteò, J. Magn. Magn. Mater. Vol-322, No.19, pp. 2908-2914, (2010).

[16] B. D. Cullity, ñIntroduction to Magnetic Materialsò, Addison-Wisley Publishing Company, Inc., California, (1972).

[17] Abbas, S.M. ñPreparation and characterization of microwave absorbing materialsò, Doctor Thesis, Indian Institute of Technology Delhi India, pp. 19ï 32, (2007).

[18] Smit, J. and Wijn, H.PJ., in: Ferrite: Physical Properties of Ferromagnetic Oxide in Relation to their Technical Application, Philips Technical library, Netherland, pp. 176ï 210 (1959).

[19] Aulock, W.H. V. ñIn: Hand book of Microwave Ferrite Materialsò, Academic Press, London, pp. 451ï 511(1965).

[20] Kohn, J.A., Eckart, D.W., and Cook, C.F., ñCrystallography of the hexagonal ferritesò. Science. 172, No. 3983, pp. 519-525, (1971).

[21] Pollert, E. ñCrystal chemistry of magnetic oxides Part 2: Hexagonal ferritesò, Prog. Cryst. Growth Charact. 11, pp.155 (1985).

[22] Wahab, M.A., ñSolid State Physics: Structure and Properties of Materialsò, Narosa Publishing House, New Delhi (1999).

[23] Dekker, A.J. ñSolid State Physicsò, Macmillan India Ltd., New Delhi (1998).

[24] Chikazumi, S. ñPhysics of Magnetismò, Jhon Wiley & Sons, Inc., New York (1966).

[25] Valenzuela, R. ñMagnetic Ceramicsò, Cambridge University Press, Cambridge (1994).

[26] Kittel, C. ñIntroduction to Solid State Physicsò, 7th edition, Jhon Wiley & Sons, Inc., Singapore (1996).

[27] Goldman, A. ñHandbook of Modern Ferromagnetic Materialsò, Kulwer Acad. Pub,

Boston, U.S.A (1999).

[28] Snoek, J.L. ñDispersion and absorptions in magnetic ferrites at frequencies above Mc/s,ò Physica, Vol-14, No.4,-217, pp.207 (1948).

[29] Yan, M.F. and Johnson, D.W. ñImpurity induced exaggerated grain growth in Mn-Zn ferrites,ò J. Am. Ceram. Soc., Vol-61, No. 7-8, 342-349, (1978).

[30] Hadfield, D. Permanent Magnets and Magnetism, Jhon Wiley & Sons, Inc., New York (1962).

[31] Sikder, S.S. ñTemperature dependence of magnetization and induced magnetic anisotropy of some Fe, Co and Ni-based amorphous ribbons,ò Ph. D. Thesis, BUET, Bangladesh (1999).

[32] Hussain, K. M. A. ñStudty of complex permeability and secondary effects in some cobalt and manganese based ferrites,ò M. Phil. Thesis, BUET, Bangladesh, (2003).

CHAPTER 3
SAMPLE PREPARATION AND STRUCTURAL CHARACTERIZATION

In this chapter the basic experimental methods and techniques to measure the lattice parameters and frequency dependent AC permeability of ferrite sample are discussed. The experimental technique for the measurement of temperature dependent initial permeability is also discussed. The Curie temperatures of the samples were determined from this temperature dependent initial permeability.

3.1 Introduction

A goal common to all the ferrites is the common formation of the spinel structure. Today, the large majority of ferrite powders are made by the conventional Ceramic process or Solid State Reaction method. Most non-conventional process involves producing the powder by a wet method. Among these methods, some are [1]:

1) Co-precipitation
2) Organic precursors
3) Sol-gel synthesis
4) Spray-drying
5) Freeze-drying
6) Combustion synthesis
7) Glass crystallization

In this chapter, we describe the solid state reaction method that is used in this research work.

3.2 Conventional Solid State Reaction Method

In the solid state reaction method, the required composition is usually prepared form the appropriate amount of raw mineral oxides or carbonates by crushing, grinding and milling. The most common type of mill is the ball mill, which consists of a lined pot with hard spheres or rod inside. Milling can be carried out in a wet medium to increase the degree of mixing. This method depends on the solid state inter-diffusion between the raw materials.

Solids do not usually react at room temperature over normal time scales. Thus it is necessary to heat them at higher temperatures for the diffusion length $(2Dt)^{1/2}$ to exceed the particle size, where D is the diffusion constant for the fast-diffusing species, and t is the firing time. The ground powders are then calcined in air or oxygen at a temperature above 1000ºC. For some time, this process is continued until the mixture is converted into the correct crystalline phase. The calcined powders are again crushed into fine powders. The pellets or toroid shaped samples are prepared from these calcined powders using die-punch assembly or hydrostatic or isostatic pressure. Sintering is carried out in the solid state, at temperature ranging 1100-1400ºC, for times of typically 1-40 h and in various atmospheres (e.g. Air, O_2 and N_2) [3-6]. Fig. 3.1 shows, diagrammatically, the stages followed in ferrite preparation.

The general solid state reaction leading to a hexaferrite $Ba_4Me_2Fe_{36}O_{60}$ may be represented as

$$2MeO + 18\,Fe_2O_3 + 4BaCO_3 \longrightarrow Ba_4Me_2Fe_{36}O_{60} + 4CO_2 + 3O_2 \text{ (U-type hexaheffite)}$$

where *Me* is the divalent ions. There are basically four steps in the preparation of ferrite:

1) Preparation of materials to form an intimate mixture with the metal ions in the ratio which they will have in the final product,
2) Heating of this mixture to form the ferrite (often called calcining),
3) Grinding the calcined powders and pressing the fine powders into the required shape, and
4) Sintering to produce a highly densified product.

3.3 Details of Calcining, Pressing and Sintering

Calcining is defined as the process of obtaining a homogeneous and phase pure composition of mixed powders by heating them for a certain time at a high temperature and then allowing it to cool slowly to discard the unwanted CO_2 and O_2. During the calcining stage, the reaction of Fe_2O_3 with metal oxide (say, *MeO* and $BaCO_3$) takes place in the solid state to form spinel according to the reactions [7]:

$$2NiO + 18\,Fe_2O_3 + 4BaCO_3 \longrightarrow Ba_4Ni_2Fe_{36}O_{60} + 4CO_2 + 3O_2 \text{(U-type hexaheffite)}$$

After that *Zn* ions are introduced by

$$(2\text{-}x)NiO + xZnO + 18\,Fe_2O_3 + 4BaCO_3 \longrightarrow Ba_4Ni_2Fe_{36}O_{60} + 4CO_2 + 3O_2$$

The calcining process can be repeated several times to obtain a high degree of homogeneity. The calcined powders are crushed into fine powders. The ideal characteristics of fine powders are [2]:

1) small particle size (sub micron)
2) narrow distribution in particle size
3) dispersed particles
4) equiaxed shape of particles
5) high purity
6) homogeneous composition.

A small particle size of the reactant powders provides a high contact surface area for initiation of the solid state reaction; diffusion paths are shorted, leading to more efficient completion of the reaction. Porosity is easily eliminated if the initial pores are very small. A narrow size distribution of spherical particles as well as a dispersed state is important for compaction of the powder during grain-body formation. Grain growth during sintering can be better controlled if the initial size is small and uniform.

A binder is usually added prior to compaction, at a concentration lower than 5wt % [2]. Binders are polymers or waxes; the most commonly used binder in ferrite is polyvinyl alcohol. The binder facilitates the particles flow during compacting and increases the bonding between the particles, presumably by forming bonds of the type *particle-binder-particle*. During sintering, binders decompose and are eliminated from the ferrite. Pressures are used for compacting very widely but are commonly several tons per square inch (i.e., up to 10^8 N m^{-2}).

Sintering is defined as the process of obtaining a dense, tough body by heating a compacted powder for a certain time at a temperature high enough to significantly promote diffusion, but clearly lower than the melting point of the main component. The driving force for sintering is the reduction in surface free energy of the powder. Part of this energy is transferred into interfacial energy (grain boundaries) in the resulting polycrystalline body [2, 8]. The sintering time, temperature and the furnace atmosphere play very important role on the magnetic property of ferrite materials. The purposes of sintering process are:

1) to bind the particles together so as to impart sufficient strength to the product,
2) to densify the material by eliminating the pores and
3) to homogenize the materials by completing the reactions left unfinished in the calcining step.

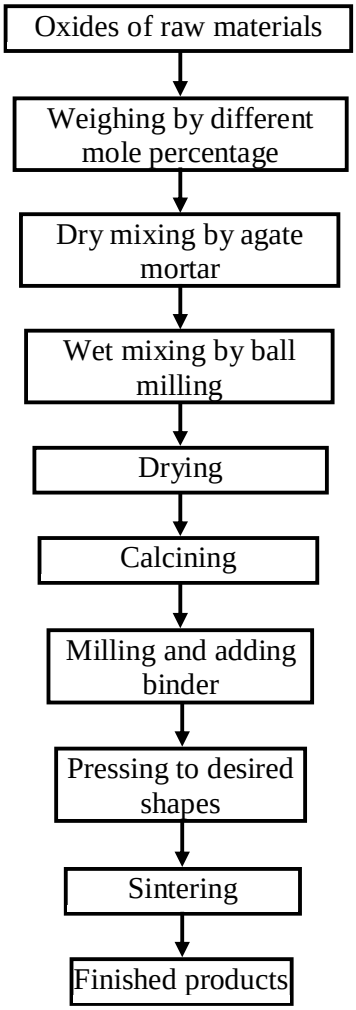

Fig. 3.1. Flow chart of the stages in preparation of spinel ferrite

Sintering of crystalline solids is dealt by Coble and Burke [9] who found the following empirical relationship regarding rate of grain growth:

$$\bar{d} = kt^n$$

where $\bar{d}$ is the mean grain diameter, n is about 1/3, t is sintering time and k is a temperature dependent parameter. Sintering is divided into three stages, Fig. 3.2 [2, 10].

Stage 1. Contact area between particles increases,

Stage 2. Porosity changes from open to closed porosity,

Stage 3. Pore volume decreases; grains grow.

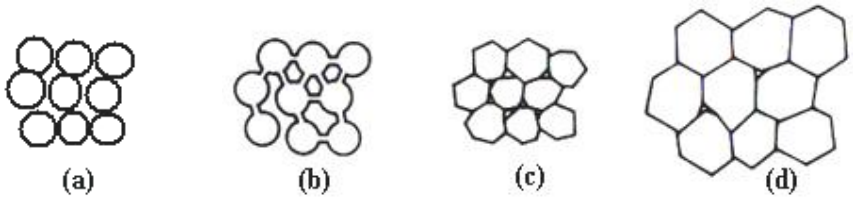

Fig. 3.2. Schematic representation of sintering stages: (a) grain-body, (b) initial stage, (c) intermediate stage, and (d) final stage.

In the initial stage, neighbouring particles form a neck by surface diffusion and presumably also at high temperatures by an evaporation-condensation mechanism. Grain growth begins during the intermediate stage of sintering. Since grain boundaries are the sinks for vacancies, grain growth tends to decrease the pore elimination rate due to the increase in distance between pores and grain boundaries, and by decreasing the total grain boundary surface area. In the final stage, the grain growth is considerably enhanced and the remaining pores may become isolated.

3.4 Preparation of the Present Samples

Polycrystalline $Ba_4Ni_{2-x}Zn_xFe_{36}O_{60}$ *(0.0≤x≤1.2 in the step of o.2)* samples were synthesized using the standard solid state reaction technique which is discussed in section 3.2. High purity powders of NiO (99.9%), ZnO (99.9%), Ba_2O_3 (99.9%), Fe_2O_3 (99.9%), will be mixed thoroughly in an appropriate amount. Mixing will be performed in the ball mill, which consists of a lined pot with hard spheres or rods inside. Milling can be carried out in a wet medium to increase the degree of mixing. The mixed powders will be calcined at 1000^0C for 5 hours. For some time this process is continued until the mixture is converted into the correct crystalline phase. The calcined powders are again crushed into fine powders. The toroid and disk shape samples (Fig. 3.3.) will be prepared from these calcined powders using uniaxial or isostatic pressure and will be sintered at temperatures between 1250-1350ºC in air for 6 hours.

Fig. 3.3. Sample (a) disk shaped, (b) toroid shaped.

3.5 X-ray Diffraction

Bragg reflection is a coherent elastic scattering in which the energy of the X-ray is not changed on reflection. If a beam of monochromatic radiation of wavelength λ is incident on a periodic crystal plane at an angle θ and is diffracted at the same angle as shown in Fig. 3.4, the Bragg diffraction condition for X-rays is given by

$$2d\,Sin\theta = n\lambda \qquad (3.1)$$

where *d* is the distance between crystal planes and *n* is the positive integer which represents the order of reflection. Equation (3.1) is known as Bragg law. This Bragg law suggests that the diffraction is only possible when λ Ò 2*d* [11]. For this reason we cannot use the visible light to determine the crystal structure of a material. The X-ray diffraction (XRD) provides substantial information on the crystal structure.

X-ray diffraction was carried out with an X-ray diffractometer for the samples. For this purpose monochromatic *Cu-*K_α radiation was used. The lattice parameter for each peak of each sample was calculated by using the formula

$$\frac{1}{d_{hkl}} = \left[\frac{4}{3}\left(\frac{h^2+hk+k^2}{a^2}\right)+\frac{l^2}{c^2}\right]^{\frac{1}{2}} \qquad (3.2)$$

where *h*, *k* and *l* are the indices of the crystal planes. The theoretical density ρ_{th} was calculated using following expression:

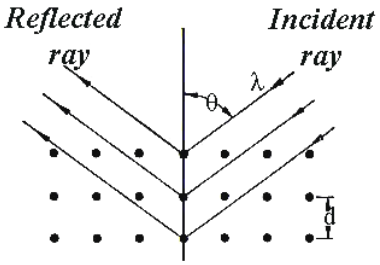

Fig. 3.4. Bragg law of diffraction.

$$d_{th} = \frac{2nM}{\sqrt{3}N_A a^2 c} g/cm^3 \qquad (3.4)$$

where n is the number of molecules per unit cell, N_A is Avogadro's number (6.02×10^{23} mol^{-1}), M is the molecular weight. The porosity was calculated from the relation $\{100(d_{th} - d_{\exp})/d_{th}\}\%$, where $d_{\exp}$ is the bulk density measured by the formula $d_{\exp} = M/V$ [12].

3.6 Microstructural Investigation

The microstructural study of the $Ba_4Ni_{2-x}Zn_xFe_{36}O_{60}$ *hexa*ferrite samples was performed in order to have an insight of the grain structures. The samples of different compositions and sintered at different temperatures were chosen for this purpose. The samples were visualized under a high-resolution optical microscope and then photographed. Average grain sizes (grain diameter) of the samples were determined from optical micrographs by linear intercept technique [3]. To do this, several random horizontal and vertical lines were drawn on the micrographs. Therefore, we counted the number of grains intersected and measured the length of the grains along the line traversed. Finally the average grain size was calculated.

3.7 Complex Permeability Measurement

For high frequency application, the desirable property of a ferrite is high permeability with low loss. One of the most important goals of ferrite research is to fulfill this requirement. The techniques of permeability measurement and frequency characteristics of the present samples are described in sections 3.7.1 and 3.7.2.

3.7.1 Techniques for the Permeability Measurement

Measurements of permeability normally involve the measurements of the change in self-inductance of a coil in presence of the magnetic core. The behavior of a self-inductance can now be described as follows. We assume an ideal loss less air coil of inductance L_0. On insertion of a magnetic core with permeability μ, the inductance will be μL_0. The complex impedance Z of this coil [1] can be expressed as follows:

$$Z = R + jX = j\omega L_0 \mu = j\omega L_0 (\mu' - j\mu'') \quad (3.5)$$

where the resistive part is $R = \omega L_0 \mu''$ (3.6)

and the reactive part is $X = \omega L_0 \mu'$ (3.7)

The RF permeability can be derived from the complex impedance of a coil, *Z*, given by equation (3.5). The core is taken as toroidal to avoid demagnetizing effects. The quantity L_o is derived geometrically as shown in section 3.7.2.

3.7.2 Frequency Characteristic Measurement

The frequency characteristics of the $Ba_4Ni_{2-x}Zn_xFe_{36}O_{60}$(0.0ÒxÒ1.2 in the step of o.2) hexaferrite samples i.e. the initial permeability spectra were investigated using an Agilent Impedance Analyzer (model no. 4192A). The complex permeability measurements on toroid shaped specimens were carried out at room temperature on all the samples in the frequency range 1 kHz - 120 MHz. The real part (μ_i') and imaginary part (μ_i'') of the complex permeability were calculated using the following relations [4]: $\mu_i' = L_s / L_0$ and $\mu_i'' = \mu_i' \tan\delta$, where L_s is the self-inductance of the sample core and $L_0 = \mu_o N^2 S / \pi\bar{d}$ is derived geometrically. Here L_o is the inductance of the winding coil without the sample core, *N* is the number of turns of the coil (*N* = 5), *S* is the area of cross section of the toroidal sample as given below:

$$S = d \times h,$$

where $$d = \frac{d_2 - d_1}{2},$$

$d_1 =$ Inner diameter,
$d_2 =$ Outer diameter,
$h =$ Height

and $\bar{d}$ is the mean diameter of the toroidal sample as given below:

$$\bar{d} = \frac{d_1 + d_2}{2}$$

The relative quality factor is determined from the ratio $\frac{\mu_i'}{\tan\delta}$.

3.8 DC Magnetization measurement

The magnetization (M) measurements were made on pieces of the samples (approximate dimensions 2 × 1 × 1 mm^3) using the Superconducting Quantum Interface Device (SQUID) magnetometer (MPMS-5S; Quantum design Co. Ltd.).

References

[1] Goldman, A. ñHandbook of Modern Ferromagnetic Materialsò, Kulwer Acad. Pub, Boston, U.S.A (1999).

[2] Valenzuela, R., ñMagnetic Ceramicsò, Cambridge University Press, Cambridge (1994).

[3] Akther Hossain, A. K. M., ñInvestigation of colossal magnetoresistance in bulk and thick film magnetites,ò Ph. D. Thesis, Imperial College, London (1998).

[4] Cullity, B.D., ñIntroduction to Magnetic Materialsò, Addison-Wisley Publishing Company, Inc., California (1972).

[5] Brook, R.J., ñSintering: An Overview, Concise Encyclopedia of Advanced Ceramic Materialsò, Pergamon Press, Oxford, pp. 438 (1991).

[6] Reijnen, P., Science of Ceramics, Academic Press, London (1967)

[7] Slick, P.I., ñFerrites for Non-microwave Applicationsò, Vol. 2, North Holland Pub. Co. (1980).

[8] Kingery, W.D., Bowen H.K. and Uhlman D.R., ñIntroduction to Ceramicsò, 2nd edition, Wiley Interscience, Newyork, pp. 476 (1976).

[9] Coble, R. L. and Burke, V., 4th Int. Symp. On the Reactivity of Solids, Amsterdam, pp. 38-51 (1960).

[10] McColm, I. J. and Clark, N. J., ñForming, Shaping and Working of high Performance Ceramicòs, Blackie, Glasgow, pp. 1-338 (1988).

[11] Kittel, C., ñIntroduction to Solid State Physicsò, 7th edition, Jhon Wiley & Sons, Inc., Singapore (1996).

[12] Cullity, B.D., ñIntroduction to Magnetic Materialsò, Addison-Wisley Publishing Company, Inc., California (1972).

CHAPTER 4

RESULTS AND DISCUSSION

The polycrystalline $Ba_4Ni_{2-x}Zn_xFe_{36}O_{60}$ (0.0≤x≤1.2 in the step of o.2) hexaferrites are studied. The hexaferrite series have been prepared using conventional solid state reaction route. Microstructural variations with composition have been found with X-ray diffraction (XRD) and optical microscope. Different U-type-hexaferrite samples are sintered at various temperatures (1250- 1350℃) for six hours. The role of sintering temperature on the mechanism of U-type hexaferrites formation is discussed. Pellets and ring shaped samples were prepared from this powder. Samples were sintered at various temperatures. Internal structure of the above mentioned samples sintered at 1250 ℃ are studied by x-ray diffraction. The DC magnetic properties were studied by SQUID magnetometer. Complex permeability of the U-type hexaferrite series $Ba_4Ni_{2-x}Zn_xFe_{36}O_{60}$ have been examined in the frequency range frequency from 0.1-120MHz.

4.1 X-ray diffraction

X-ray diffraction (XRD) pattern for various $Ba_4Ni_{2-x}Zn_xFe_{36}O_{60}$ (0.0ÒxÒ1.2 in the step of o.2) U-type hexagonal ferrites are shown in Fig.4.1. All peaks observed in the XRD patterns are identified with their Miller indices. The XRD patterns for these compositions confirm the formation of U-type hexaferrite with a few impurity peaks [1]. The impurity peaks are mainly from the unreacted ingredients of these compositions. The lattice parameters ‘a’ and ‘c’ of $Ba_4Ni_{2-x}Zn_xFe_{36}O_{60}$ compositions are plotted as a function of Zn content, as shown in Fig. 4.2. It is observed from the figure that the variation of lattice parameters ‘*a*’ and ‘c’ increases with *Zn* content in the $Ba_4Ni_{2-x}Zn_xFe_{36}O_{60}$.Similar behavior was observed by Meena et al. [2] for $Ba_4Mn_{2-x}Zn_xFe_{36}O_{60}$ hexaferrite. The increase in lattice parameter with increasing Zn content can be explained on the basis of the ionic radii. The ionic radii of the cations used in $Ba_4Ni_{2-x}Zn_xFe_{36}O_{60}$ are 0.83Å (Ni^{2+}), 0.88Å (Zn^{2+}) and 0.69Å (Fe^{3+}) [3]. Since the ionic radius of Ni^{2+} is less than that of the Zn^{2+}, increase in lattice constant with the increase in *Zn* substitution is expected. The lattice parameter ‘*a*’ *and* ‘*c*’ of $Ba_4Ni_{2-x}Zn_xFe_{36}O_{60}$ compositions are plotted as a function of *Zn* content, as shown in Fig. 4.2.

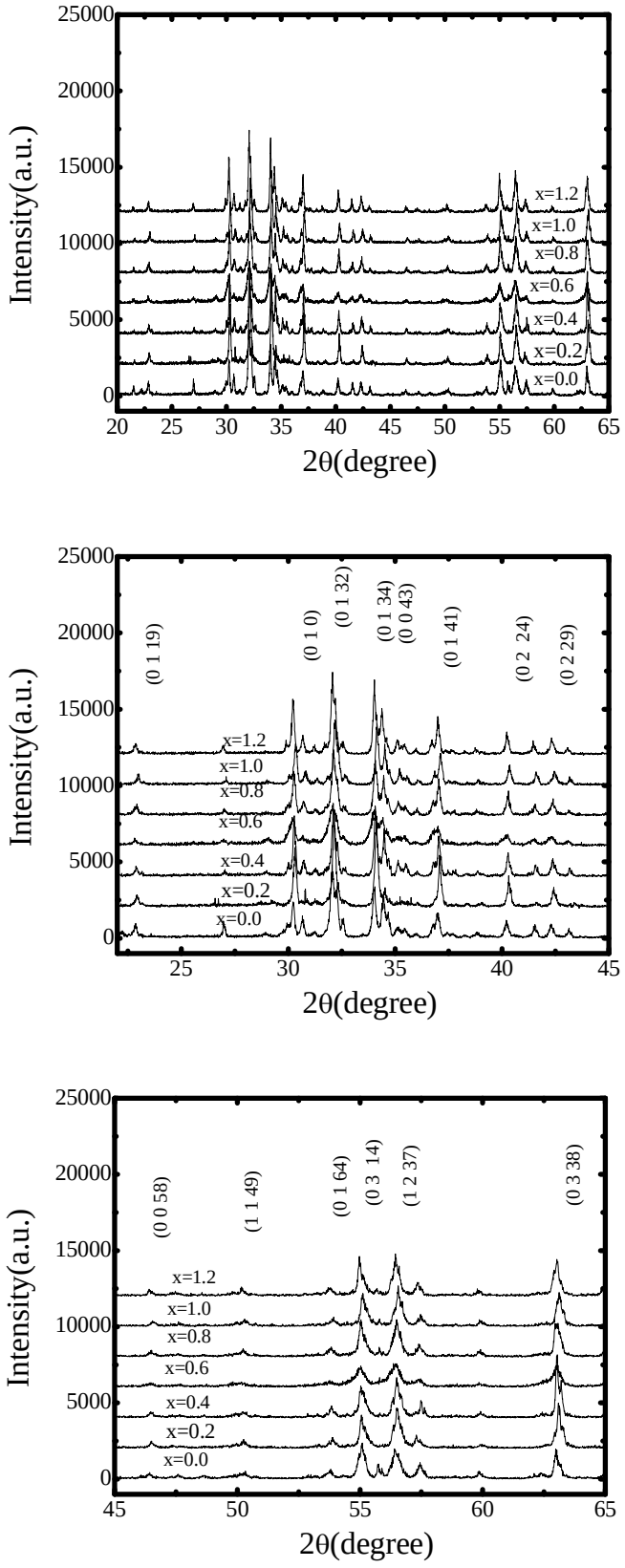

Fig. 4. 1. X-ray diffractogram (XRD) for different compositions.

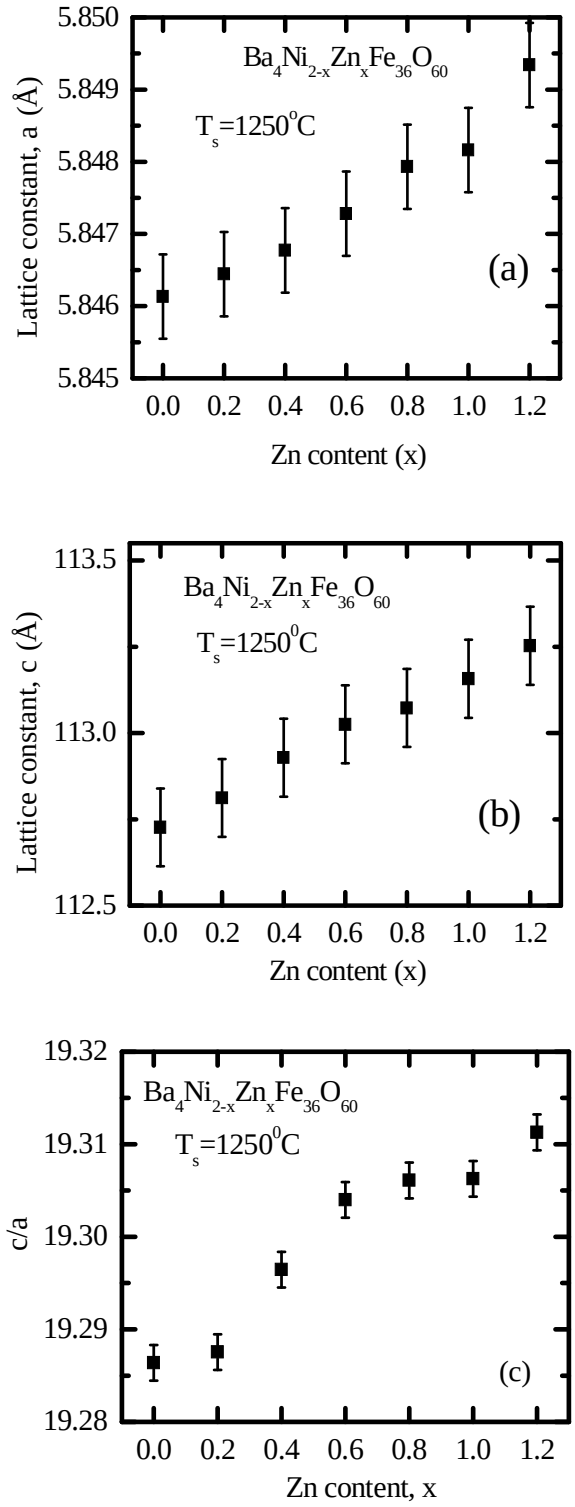

Fig. 4. 2. Variation of lattice parameter (a) ά*a*ô (b) ά*c*ô (c) c/a with Zn content ά*x*ô of polycrystalline $Ba_4Ni_{2-x}Zn_xFe_{36}O_{60}$ *hexaferrites*

4.2 Density and porosity

Fig.4.3 shows the experimental density (d_{exp}) of the samples and is observed to be increasing with increasing of Zn content. This increase in density with increasing Zn content can be explained on the basis of the atomic weight. Since the atomic weight of *Ni* (47.88 amu) is less than that of Zn (65.39 amu) therefore increase in density is expected. Fig.4.4 shows the experimental density and porosity as a function of *Zn* content of the samples sintered at 1250°C.

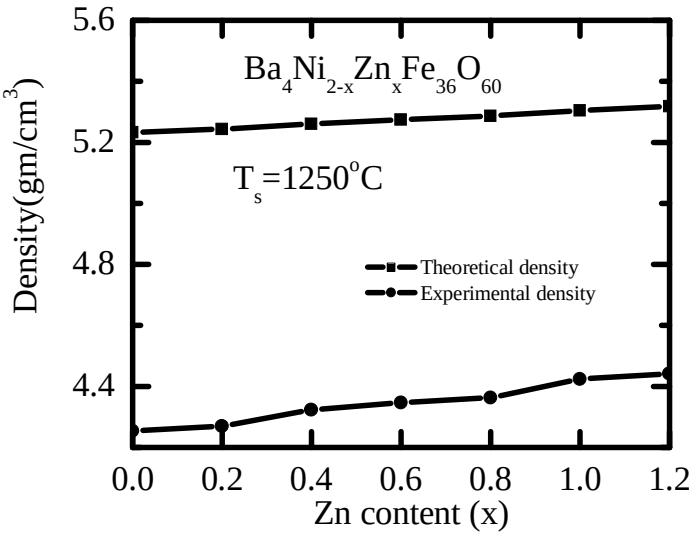

Fig. 4.3. Variation of x-ray density (d_{th}) and experimental density (d_{exp}) with Zn content *'x*ô of polycrystalline $Ba_4Ni_{2-x}Zn_xFe_{36}O_{60}$ *hexaferrites*

During the sintering process, the thermal energy generates a force that drives the grain boundaries to grow over pores, thereby decreasing the pore volume and increasing the density of the material. It is known that the porosity of ceramic samples results from two sources, intragranular porosity and intergranular porosity [4]. Thus the total porosity could be written as $P=P_{intra}+P_{inter.}$ The intergranular porosity mainly depends on the grain size [4]. At higher sintering temperatures the density decreases because the intragranular porosity increases resulting from discontinuous grain growth.

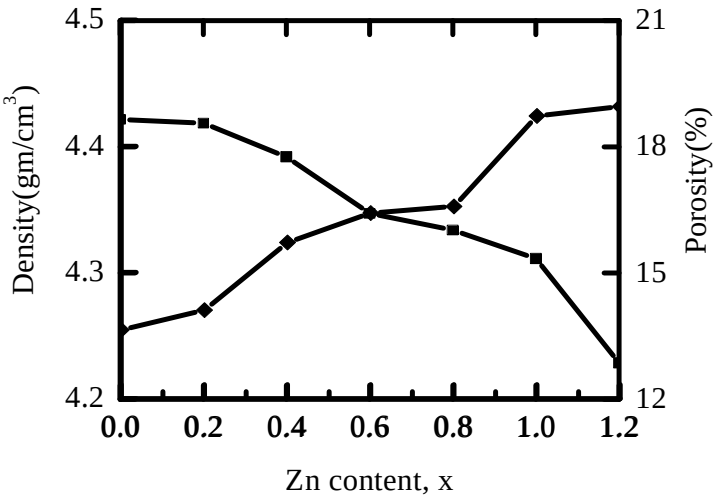

Fig. 4.4. Variation of experimental density and porosity with Zn content óxô polycrystalline $Ba_4Ni_{2-x}Zn_xFe_{36}O_{60}$ samples sintered at 1250ºC

4.3 Microstructures of polycrystalline $Ba_4Ni_{2-x}Zn_xFe_{36}O_{60}$

Fig.4.5 shows the microstructures for polycrystalline $Ba_4Ni_{2-x}Zn_xFe_{36}O_{60}$ compositions. The average grain size increases with the increase of Zn content. It is observed that the sample composition has an influence on the enhancement of grain size. Normally *Zn* lowers sintering temperature and promotes grain growth. In this case, as *Zn* content increases and *Ni* content decreases so the grain size also increases. The grain size reflects the presence of more or less grain boundary area. Even porosity may be strongly related to boundaries since they can remove porosity. The uniformity in the grain size and the average grain diameter can control properties such as the magnetic permeability. When the grain growth rate is very high, pores may be left behind by rapidly moving grain boundaries, resulting in pores that are trapped inside the grains. This intragranular porosity is practically impossible to eliminate, leading to poor magnetic and mechanical properties.

The driving force for grain growth is the surface tension of the grain boundary [5]. The interaction of grain boundary and porosity along with sintering temperature is important in determining the limiting grain size [6].When many pores are present and the sintering temperature is not too high for certain composition, grain growth is inhibited. Once the porosity has decreased to a value such that secondary grain growth can occur, extensive grain

growth may result if the sintering temperature is too high for certain composition. As a result, many pores become isolated from grain boundaries, and the diffusion distance between pores and grain boundary becomes large.

The behaviour of grain growth reflects the competition between the driving force for grain boundary movement and the retarding force exerted by pores [7]. When the driving force of the grain boundary in each grain is homogeneous, the sintered body attains a uniform grain size distribution; in contrast, discontinuous grain growth occurs if this driving force is inhomogeneous. The discontinuous growth of grain rises with temperature, hindering the migration of the pore to the grain boundary and hence, contributing toward the reduction of the sintered density.

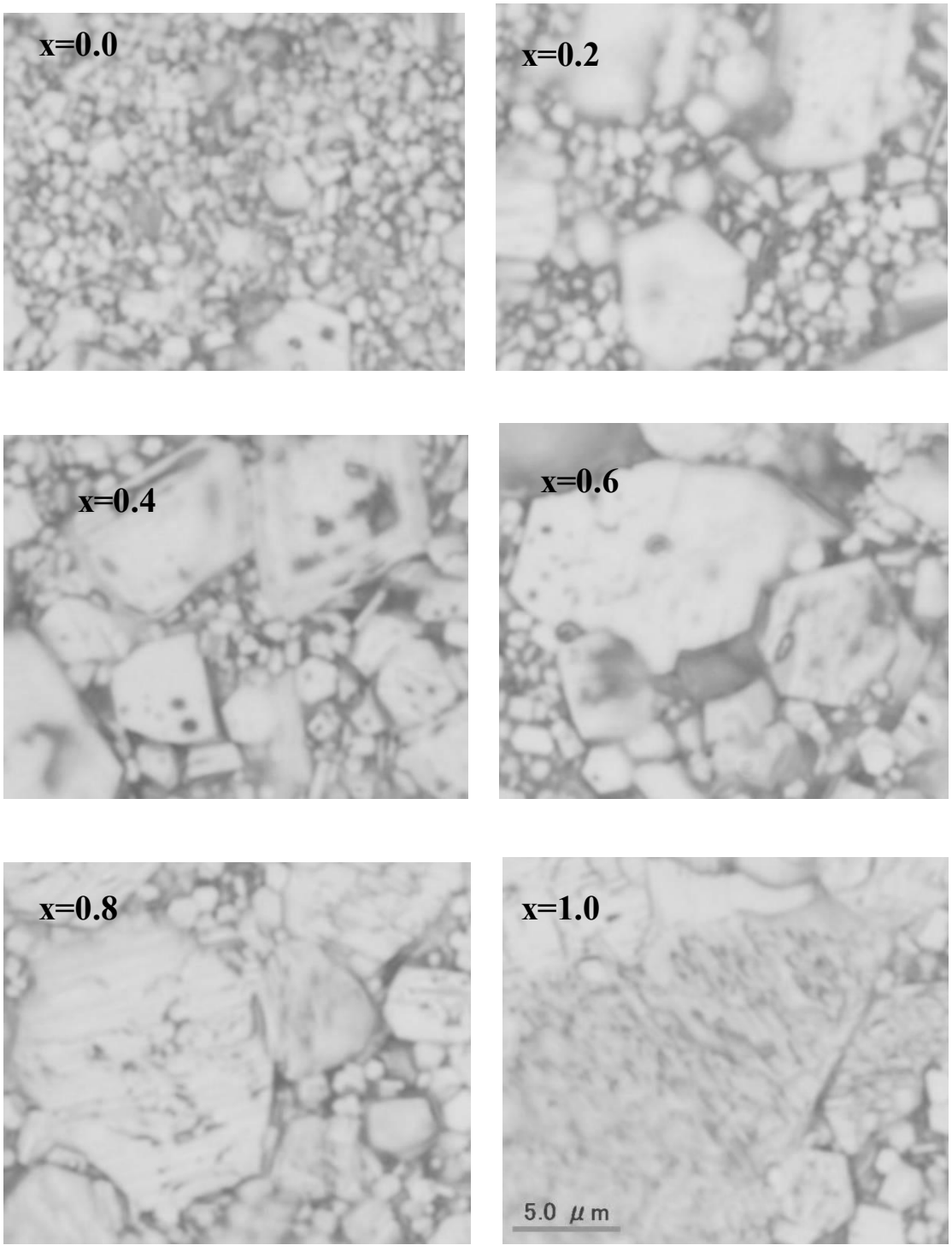

Fig. 4.5. The optical micrographs of the polycrystalline $Ba_4Ni_{2-x}Zn_xFe_{36}O_{60}$ samples sintered at temperatures 1250ºC in air

4.4 Complex permeability

The complex permeability is given by $\mu^* = \mu' - i\mu''$, where μ' and μ'' are the real and imaginary parts of initial permeability, respectively. The real permeability μ' describes the stored energy expressing the component of magnetic induction B in phase with the alternating magnetic field H. The imaginary permeability μ'' describes the dissipation of energy expressing the component of B at 90^0 out of phase with the alternating magnetic field. The frequency dependence of the complex permeability of all samples is illustrated in Figs. 4.6 to 4.8 in the range from 0.1 to 120 MHz. Initial permeability is found to increase significantly with the increase of zinc content and sintering temperature. The initial permeability of ferrite material depends on many factors like reversible domain wall displacement, domain wall bulging as well as microstructural features viz., average grain size, intra-granular porosity, etc. [8]. In a demagnetized magnetic material, there are a number of Weiss domains with Bloch walls separating two domains. These walls are bound to the equilibrium positions. It is well known that the permeability of polycrystalline ferrite is related to two magnetizing mechanisms: spin rotation and domain wall motion. [9], which can be described as follows:

$$\mu_i = 1 + \chi_w + \chi_{spin}$$

where χ_w is the domain wall susceptibility; χ_{spin} is intrinsic rotational susceptibility. χ_w and χ_{spin} may be written as : $\chi_w = 3\pi M_s^2 D/4\gamma$ and $\chi_{spin} = 2\pi M_s^2/K$ with M_s saturation magnetization, K the total anisotropy, D the average grain diameter, and γ the domain wall energy. Thus the domain wall motion is affected by the grain size and enhanced with the increase of grain size. The initial permeability is therefore a function of grain size. The magnetization caused by domain wall movement requires less energy than that required by domain rotation. As the number of walls increases with the grain sizes, the contribution of wall movement to magnetization increases. μ' decreases monotonically with frequency for all samples, and this decrease is more rapidly at low frequencies. μ' is also annealing temperature and composition dependent, which is depicted in Figs 4.6, 4.7 and 4.8. It is clear from the Figs 4.9 and 4.10 that permeability increases for all samples as the sintering temperature increases from 1250 to 1300°C and above the1300°C permeability decreases. The reason behind this is the samples heated at higher temperature contain increasing number of pores within the grain which results in decrease in permeability.

Increase in μ' with increase in sintering temperature is also observed. Higher sintering temperatures result in the increase in the density of the specimen which facilitates the movement of the spins as the numbers of pores which impede the wall motion are reduced. Increase in the sintering temperature also results in a decrease in the internal stresses, which reduce the hindrance to the movement of the domain walls resulting thereby in the increased value of μ' [10] Similar results were observed for all the studied samples [11]. However, natural resonance phenomenon is not observed in μ' for any sample within measurement frequency range.

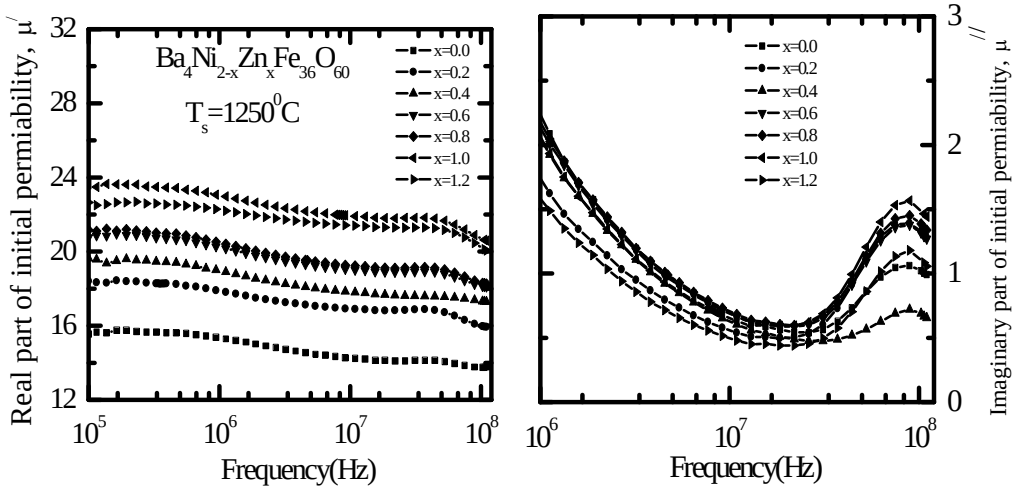

Fig. 4.6. (a) Real (b) imaginary part of initial permeability for samples sintered at temperature 1250°C for 6h

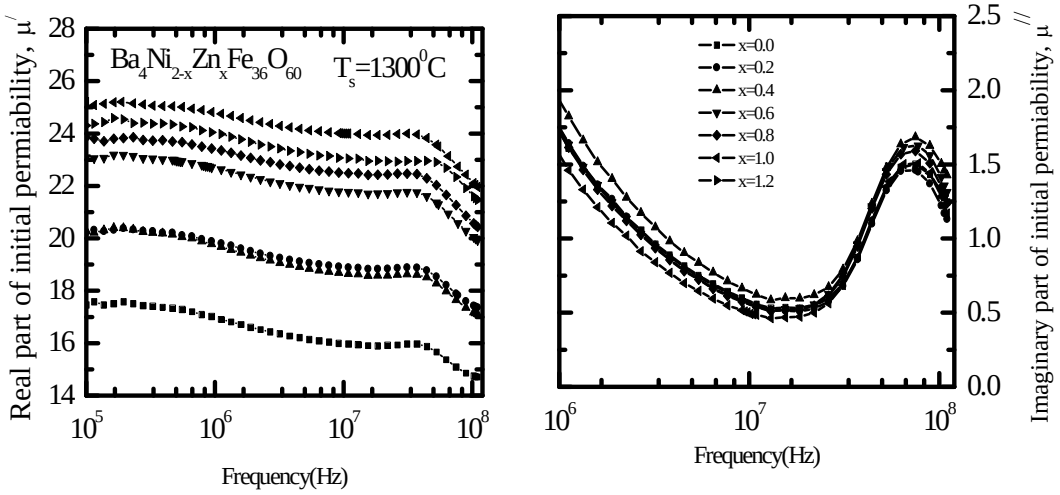

Fig.4.7. (a) Real (b) imaginary part of initial permeability for samples sintered at temperature 1300°C for 6h

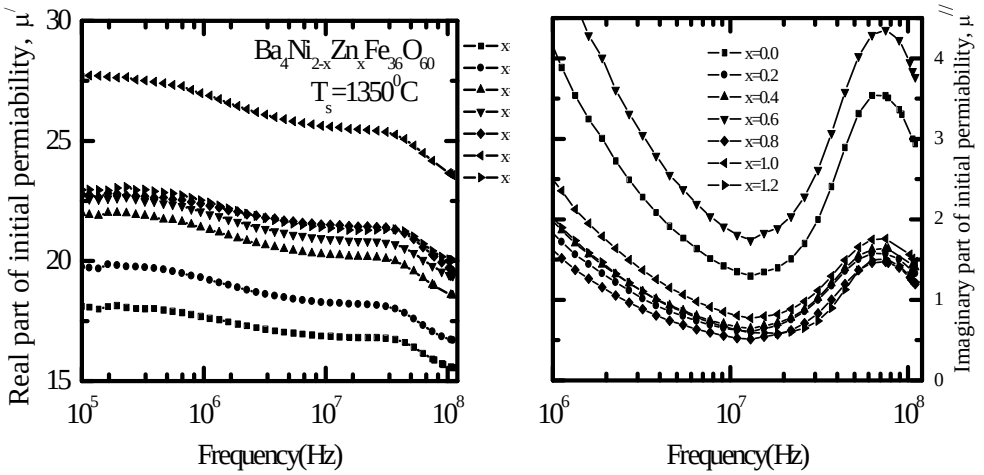

Fig. 4.8. (a) Real (b) imaginary part of initial permeability for samples sintered at temperature 1350°C for 6h

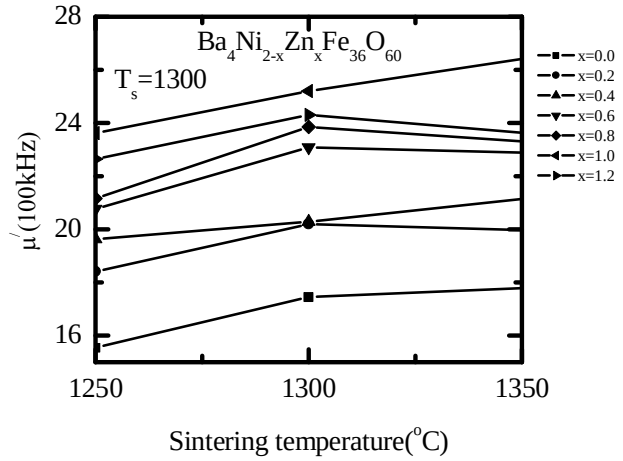

Fig. 4.9. Variation of permeability at 100kHz as function of sintering

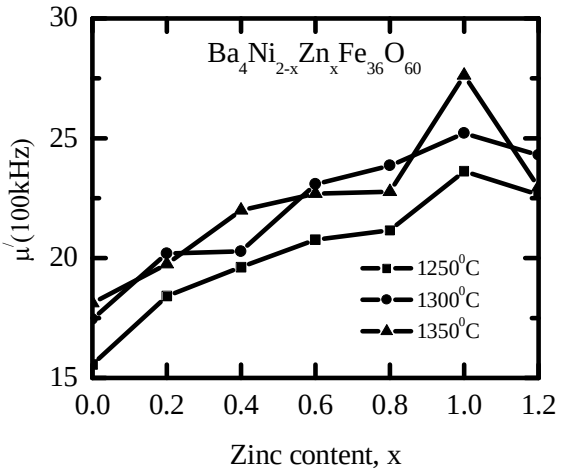

Fig. 4.10. Variation of permeability at 100kHz as Zn content

4.5 Loss factor

Energy loss is an extremely important factor in ferromagnetic materials, since the amount of energy wasted on process other than magnetization can prevent the AC applications of a given material. The ratio of $\mu_i^{/}$ and $\mu_i^{//}$ representing the losses in the material are a measure of the inefficiency of the magnetic system. Obviously this parameter should be as low as possible. The magnetic losses, which cause the phase shift, can be split up into three components: hysteresis losses, eddy current losses and residual losses. This gives the formula $\tan\delta_m = \tan\delta_h + \tan\delta_e + \tan\delta_r$. As μ_i is the initial permeability which is measured in presence of low field, therefore, hysteresis losses vanish at very low field strengths. Thus at low field the remaining magnetic losses are due to eddy current losses and residual losses. Residual losses are independent of frequency. Eddy current losses increase with frequency and are negligible at very low frequency. Eddy current loss can be expressed as $P_e \approx f^2/\rho$, where P_e is the energy loss per unit volume and ρ is the resistivity [9]. To keep the eddy current losses constant as frequency is increased; the resistivity of the material chosen must increase as the square of frequency. The ferrite microstructure is assumed to consist of grains of low resistivity separated by grain boundaries of high resistivity. Thicker grain boundaries are preferred to increase the resistance.

The variation of loss factor, *tanδ,* with frequency for the polycrystalline $Ba_4Ni_{2-x}Zn_xFe_{36}O_{60}$ compositions are shown in Fig. 4.11 to 4.13 for different sintering temperatures at 1250°C (Fig. 4.11), 130°C (Fig. 4.12) and 1350°C(Fig. 4.13), respectively.

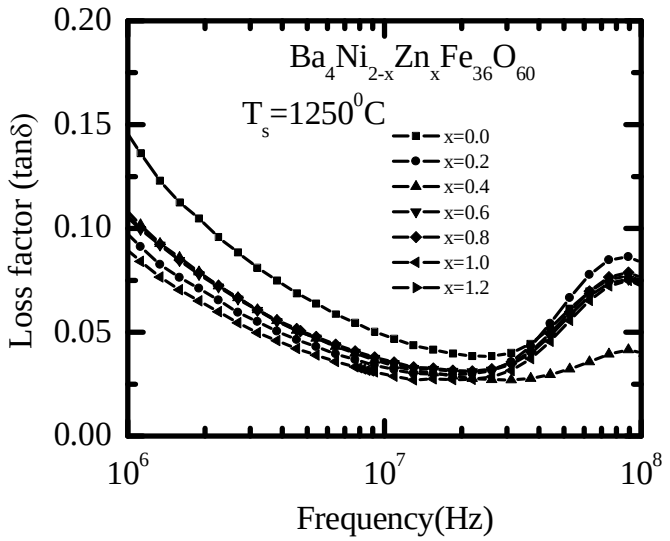

Fig. 4.11 The variation of loss factors with frequency for polycrystalline $Ba_4Ni_{2-x}Zn_xFe_{36}O_{60}$ samples sintered at 1250°C

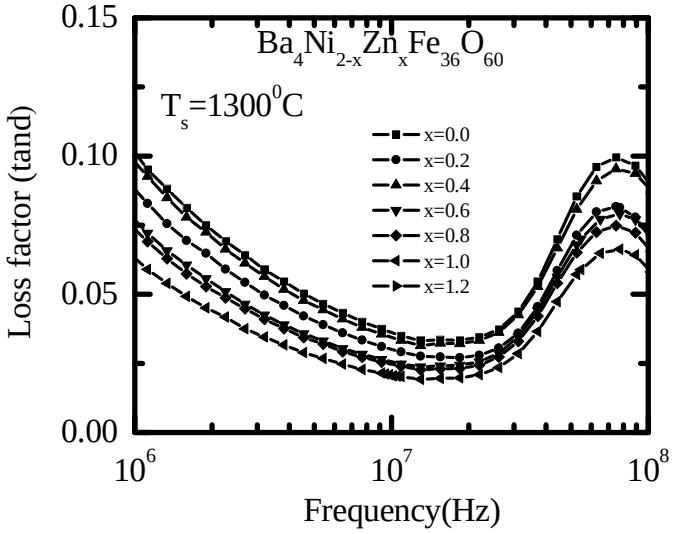

Fig. 4.12 The variation of loss factors with frequency for polycrystalline $Ba_4Ni_{2-x}Zn_xFe_{36}O_{60}$ samples sintered at 1300°C

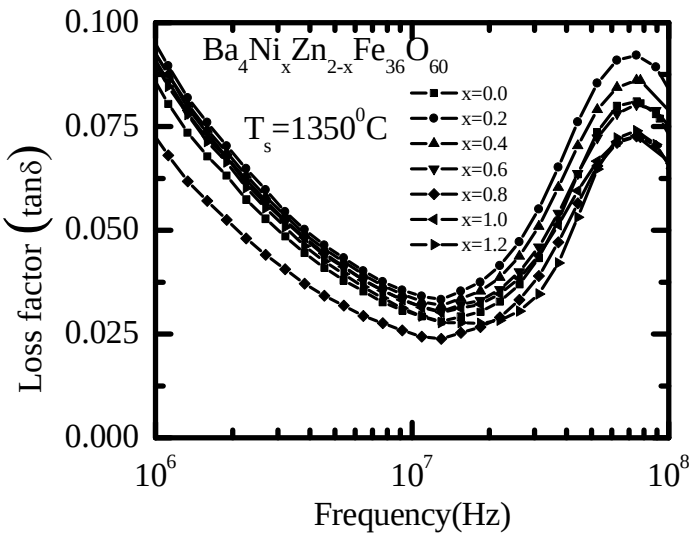

Fig. 4.13 The variation of loss factors with frequency for polycrystalline $Ba_4Ni_{2-x}Zn_xFe_{36}O_{60}$ samples sintered at 1350°C

4.6 Relative quality factor

Figs. 4.14- 4.16 show the frequency dependence of relative quality factor (RQF) of the samples sintered at 1250^0C, 1300^0C and 1350^0C. The quality factors were calculated from the magnetic loss tangent measured on the coil wound toroidal samples. The variation of the relative quality factor with frequency showed a similar trend for all the samples. Q-factor increases with an increase of frequency, showing a peak and then decreases with frequency. This happens at the frequency where the permeability begins to drop. This phenomenon is associated with the ferrimagnetic resonance within the domains [12] and at the resonance maximum energy is transferred from the applied magnetic field to the lattice resulting in the rapid decrease in RQF. But no resonance phenomenon due to domain wall rotation was observed in the permeability spectra within the measured frequency range but a small peak was observed in all samples. Thus, the observed resonance phenomenon is associated with the ferrimagnetic magnetic domain wall resonance. This type of magnetic domain wall resonance peak was found in other hexaferrites [13].

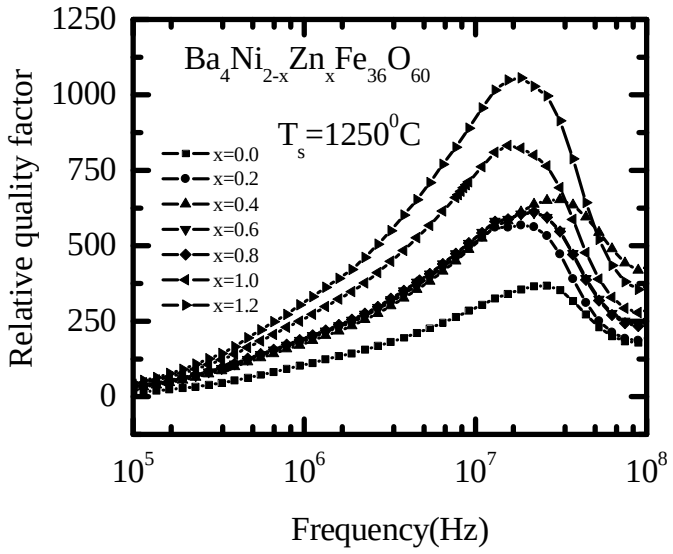

Fig. 4.14. The variation of relative *Q* factors with frequency for Fe_3O_4 sintered at 1250^0C for 6h.

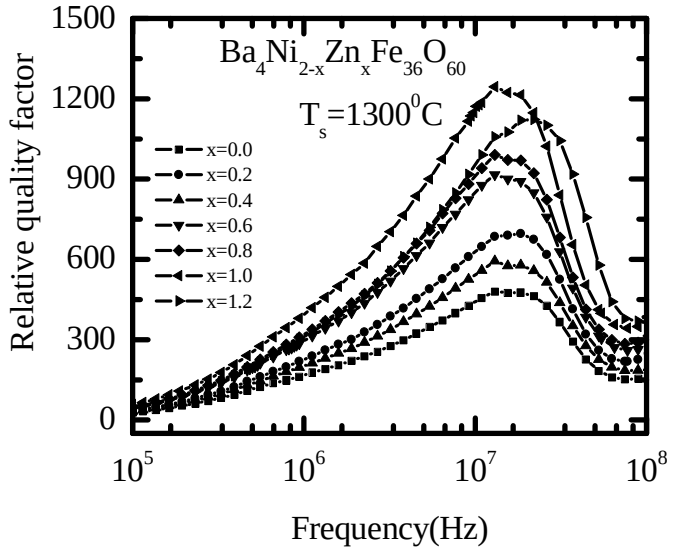

Fig. 4.15. The variation of relative *Q* factors with frequency for Fe_3O_4 sintered at 1300^0C for 6h

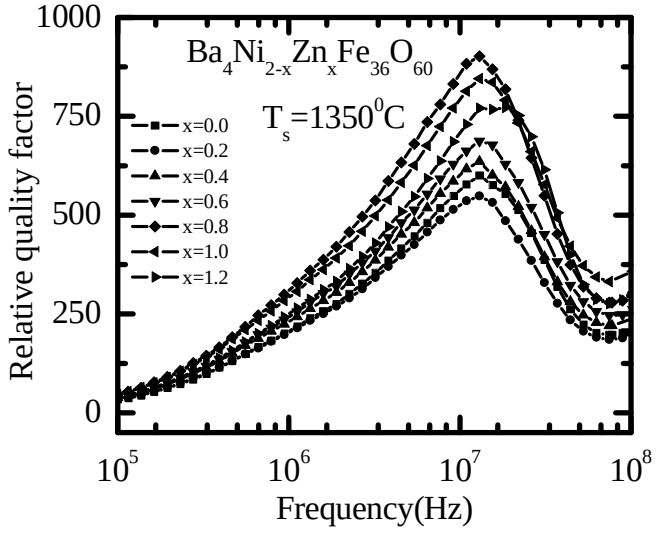

Fig. 4.16. The variation of relative *Q* factors with frequency for Fe_3O_4 sintered at 1350^0C for 6h

4.7 DC magnetization of $Ba_4Ni_{2-x}Zn_xFe_{36}O_{60}$

An intrinsic property such as saturation magnetization (M_s) is controlled by the composition whereas an extrinsic property by the microstructure that is in turns governed by the processing techniques. The magnetization of magnetic materials is a structural sensitive static property (intrinsic property), the magnetic field required to produce the saturation value varies according to the relative geometry of the field to the easy axes and other metallurgical conditions of the material.

The magnetization as a function of applied magnetic field, *M-H*, for polycrystalline $Ba_4Ni_{2-x}Zn_xFe_{36}O_{60}$ samples at room temperature (300K) is shown in Fig. 4.17. The magnetization of $Ba_4Ni_{2-x}Zn_xFe_{36}O_{60}$ samples increases linearly with increasing the applied magnetic field up to 0.5 T and attains its saturation value for fields higher than 2 Tesla except x=0 samples. The saturation magnetization of the polycrystalline $Ba_4Ni_{2-x}Zn_xFe_{36}O_{60}$ sample is above 1 Tesla.

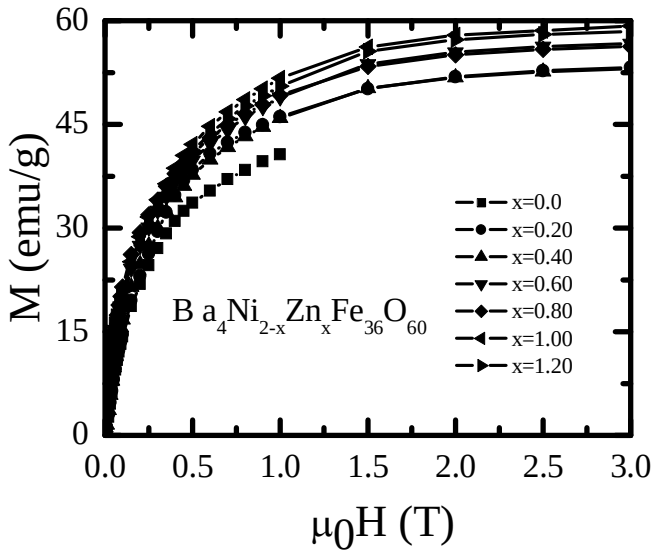

Fig. 4. 17: The magnetization as a function of applied magnetic field plots for sintered (1250ęC) samples measured at 300 K.

In low field Rayleigh region, magnetization is believed to change entirely by domain wall motion. Between the low-field Rayleigh region and the high field region near saturation there exists a large section of the magnetization curve, comprising most of the change of magnetization between zero and saturation curve, comprising most of the change of magnetization between zero and saturation. The main processes occurring here are large Barkhausen jump, and the shape of this portion of the magnetization curve varies widely from one kind of specimen to another. In high field region, on the other hand, domain rotation is predominant effect, and this phenomenon obeys fairly simple rules.

The variation of the saturation magnetization of the compositions with the Zn content is plotted in Fig 4.18. The obtained experimental values have good agreement with the study obtained Lisjak et al. [14]. It is clearly indicated that the saturation magnetization of the compositions increases with increasing Zn content.

The number of μ_B per atom for each composition is calculated using the experimental values of M_s using following relation,

$$n = \frac{M \times M_s}{N \times \mu_B}$$

Where M is the molecular weight of the specimen, N is Avogadroôs number, and μ_B is 9.27×10^{-21} emu. The number of μ_B increases with the increase of Zn content as shown in Fig. 4.19.

The observed increase of M_s, versus Zn content is consistent with the enhancement of the superexchange interaction network when diamagnetic zinc is replaced by magnetic nickel. The crystal lattice of the U-type hexaferrite consists of M-type and Y-type ferrites (2M+Y). The U-type hexaferrite compounds are ferrimagnetic at room temperature and their magnetic structure model was suggested by Gorter [l5]; all the magnetic moments are ordered in the basal plane according to the scheme given in Table1. [16, 17]. According to this current model, and locating the diamagnetic Zn^{2+} cation on the spin-down and tetrahedral sites of T- and S-blocks. In order to explain this lower value of saturation above x=1 can be explained by local spin canting with a magnetic component along the hexagonal c-axis, as proposed from Mossbauer spectroscopy [11].

Table 4.1: Cation distribution in $Ba_4Ni_{2-x}Zn_xFe_{36}O_{60}$ hexaferrite

Sublattice	**Coordination**	**Block**	**No of ions per unit cell**	**Spin**
c_{IV}	tetrahedral	S	6	Down
a_{VI}	Octahedral	S	3	Up
h_{VI}	Octahedral	T-S	18	Up
c_{VI}	Octahedral	T	6	Down
c_{VI}	Tetrahedral	T	6	Down
b_{VI}	Octahedral	T	3	Up
K	Octahedral	R-S	36	Up
f_{VI}	Octahedral	R	12	Up
A	Octahedral	S	6	Up
f_{IV}	Tetrahedral	S	12	Down
B	Five-fold	R	6	Up

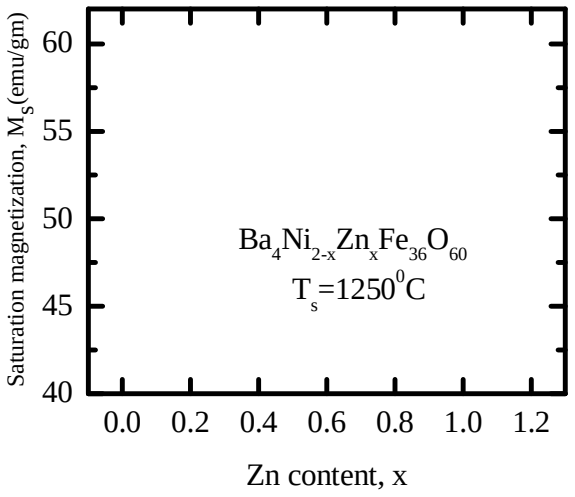

Fig. 4.18: Saturation magnetization for different values of zinc content x

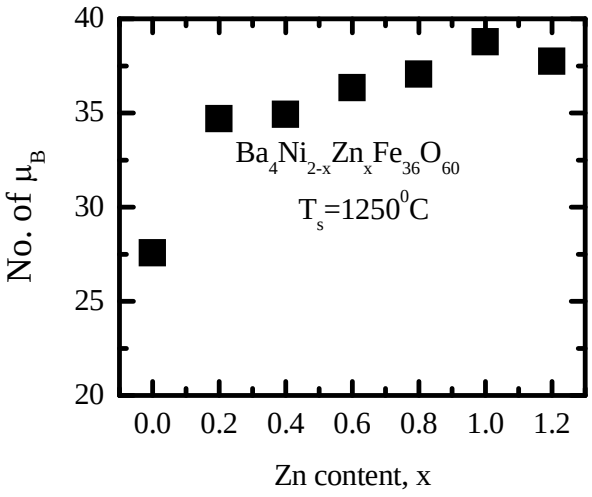

Fig. 4.19: No. of ε_B for different values of zinc content x

4.8. Dielectric constant

It was discovered by the Brockman *et al.* [18-19] that sintered hexaferrites with low resistivity at lower frequencies (below 1 MHz) have a high dielectric constant. The variation of dielectric constant (ε) with frequency (1 kHzï 1 MHz) of the $Ba_4Ni_{2-x}Zn_xFe_{36}O_{60}$ (0.0ÒxÒ1.2) samples is shown in Fig. 20. It can be seen that all the samples show the frequency-dependent phenomenon i.e., the dielectric constant decreases with increasing

frequency exhibiting a normal ferromagnetic behavior. A more dielectric dispersion is observed at lower frequency region and it remains almost independent of applied field at higher frequency region. This behavior of a dielectric may be explained qualitatively by the supposition that the mechanism of the interfacial polarization process, which occurs when charge carriers are present that can migrate an appreciable distance through the dielectric but which become trapped or cannot discharge at an electrode in ferrite is similar to that the conduction process [19]. The electrical conduction mechanism can be explained by the electron hopping model of Verway [20]. Verway explained that the electronic conduction mechanism in ferrites is mainly due to hopping mechanism of electrons between ions of the same element existing in more than one valence state and distributed randomly over crystallographically equivalent lattice sites. A number of such ions are formed during the sintering process of ferrites. Fe^{+2} ions concentration is a characteristic property of a ferrite materials and depends upon several factor such as sintering temperature, time, rate of increase of sintering temperature and atmosphere including grain structure. Creation of Fe^{+2} ions gives rise to electron hopping between Fe ions in+2 and +3 valence states. The electronic exchange between Fe^{+2} and Fe^{+3} ions results the local displacement of charge carriers in the direction of the applied electric field, which is responsible for the polarization of ferrites [21, 22]. Since Fe^{+2} ions are easily polarizable, the larger number of Fe^{+2} ions the higher would be the dielectric constant. The dielectric constant decreases with increasing frequency and then reaches almost constant value due to the fact that beyond a certain frequency of external alternating field, the electron exchange between Fe^{+2} *and* Fe^{+3} cannot follow the alternating field. All the samples have high value of ε in the order of 10^4 at low frequencies. This high value at lower frequency region is due to Maxwell-Wagner interfacial type of polarization [23] for the inhomogeneous double layer dielectric structure which is in agreement with Koops Phenomenological theory [24]. The inhomogeneous dielectric structure was supposed to be consisted by two layers. The first one is the fairly well conducting large ferrites grains which are separated by the second thin layer of the poorly conducting grain boundaries. The grain boundaries of lower conductivity and higher dielectric constant are found to be more effective at lower frequencies while the ferrite grains of higher conductivity and lower dielectric lower dielectric constant are more effective at higher frequencies [25].

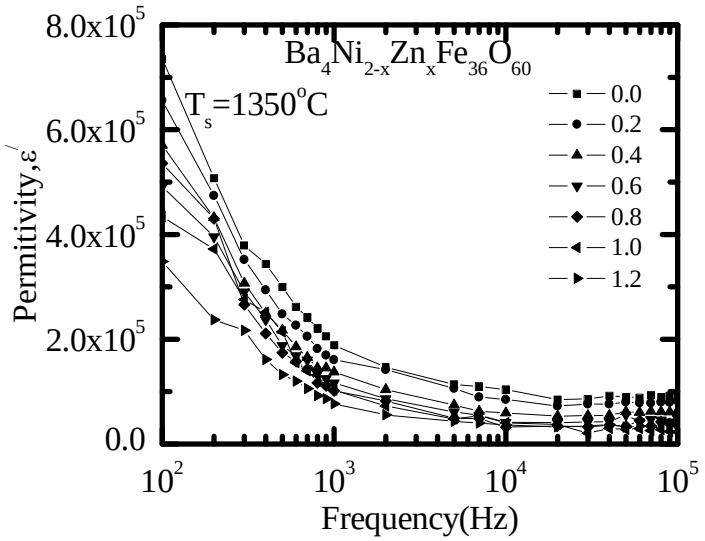

Fig. 4. 20: The dielectric constant as a function of frequency plots for sintered (1350ęC) samples

It is known that these U-type hexaferrites with complex crystalline structure consist of multiple dipoles (various cations like Ba^{2+}, Fe^{2+}, Fe^{3+}, Ni^{2+}, Zn^{2+} form dipoles at their respective positions with surrounding O^{2-} ions) with different relaxations times. In sample x=0 (Ni_2U) formation of some Ni^{4+} ions helps to convert Fe^{3+} ion into Fe^{2+} ions in order to balance the charge ($Ni^{4+}+Fe^{2+} \leftrightarrow Fe^{3+}$)[26-27]. The addition of Zn^{2+} ions seems to disturb this equilibrium and could reduce the hopping conduction in the sample. On the other hand, Zn is also volatile in nature and some percentage of it escapes during sintering leaving some vacancies in the structure. The evaporation of Zn ions during sintering, process may increase the number of Fe^{2+} ions at these sites [28-30], in turn lead to an increase in hopping conduction. Moreover, the vacant states also may lead to dielectric loss increase in the sample due to increased stress in the lattice [31-33]. Another phenomenon that dictates the conductivity behavior of the sample is the fact that Zn is known to have strong affinity for tetrahedral site; however, the Ni is present in both octahedral and tetrahedral sites owing to its possible multivalent states. Therefore, a partial substitution of Zn for Ni may dilute conduction effects occurring through tetrahedral sites. Thus, the final conduction behavior in these Zn substituted Ni hexaferrites is a fine balance between all these above mentioned processes.

References

[1] Lisjak, D., Makovec D. and Drofenik, M., ñFormation of U-type hexaferritesò, J. Mater. Res. Vol-19, No.8, pp. 2464-2469, (2004).

[2] Meena, R.S., Bhattachrya, S. and Chatterjee, R., ñComplex permittivity, permeability and microwave absorbing properties of ($Mn_{2-x}Zn_x$) U-type hexaferriteò, J. Magn. Magn. Mater. Vol-322, No. 19, pp.2908-2914, (2003).

[3] Huhecy, J.E., Keiter, E. A., and Keiter, R. L., ñInorganic Chemistry Principles of Structure and Reactivityò. 4th Edition.

[4] Sattar, A. A., El-Sayed, H. M., El-Shokrofy, K. M. and El-Tabey, M. M., ñImprovement of the magnetic properties of Mn-Ni-Zn ferrite by the non-magnetic Al^{3+} ion substitution,ò J. Appl. Sci., Vol-5, No.1, pp.162 -168, (2005).

[5] Coble, R. L., Burke, J. E., (Ed.), ñSintering in Ceramics, Progress in Ceramic Scienceò, Pergamon Press, Vol.3, pp.197, (1964).

[6] Kingery, W. D., Bowen, H. K., Uhlmann, D. R ñIntroduction to Ceramic Science, Wileyò, New York, pp.474 (1975).

[7] Costa, A.C.F.M., Tortella, E., Morelli, M.R. and Kiminami, R.H.G.A., ñSynthesis, microstructure and magnetic properties of Ni-Zn ferrites,ò J. Magn. Magn. Mater. Vol-256, No. 1-3, pp.174-182, (2003).with

[8] J. Smit, H.P.J. Wijn, Ferrites, Philips Tech. Library, Netherlands (1959).

[9] Tsutaoka, T., Ueshima, M., T. Tokunaga, Nakamura, T. and Hatakeyama, K. ñFrequency dispersion and temperature variation of complex permeability of Ni-Zn ferrite composite materials,ò J. Appl. Phys., Vol-78, No. 6, pp. 3983-39, (1995).

[10] Verma, A., Goel, T.C. and Mendiratta, R.G., ñFrequency variation of initial permeability of NiZn ferrites prepared by the citrate precursor methodò. J. Magn. Mag. Mat. Vol-210, No. 1-3, pp.274-278 (2000).

[11] Wijn, H.P.J., ñHexagonal ferrites,ò in Landolt-Börnstein Numerical Data and Functional Relationships in Science and Technology New Series, K.-H. Hellwege, Ed. New York: Spinger, pt. b, Vol-4, ch. 7, pp. 558. Group III (1970).

[12] Brockman, F.G., Dowling, P.H., and Steneck, W. G., ñDimensional Effects Resulting from a High Dielectric Constant Found in a Ferromagnetic Ferriteò, Phys. Rev. Vol-77 , No.1, pp. 85-93, (1950).

[13] Bai, Y., Zhou, J., Gui, Z., and Li, L. ñEffect of substitution on magnetization mechanism for Y-type hexagonal ferriteò, Mater. Sci. Eng. B, Vol-103, No.2, pp.115-

117, (2003).

[14] Lisjak, D. and Drofenik, M., ñThe thermal stability range and magnetic properties of U-type hexaferrites,ò J. Magn. Magn. Mater., Vol.-272-276, Supplement.1 pp. 1817-1819, (2004).

[15] Gorter, E.W., Proc. IEEE 104B, pp. 255 (1957).

[16] Bolzoni, F. and Parwt, L., ñMagnetic properties of Y-type trigonal ferrites first-order magnetization processes in trigonal systemsò, Magn. Magn. Mater. Vol-42, No.1, pp.44-52, (1984).f

[17] Sugimoto, S., Haga, K., Kagotani T., and Inomata, K.O. ñMicrowave absorption properties of Ba M-type ferrite prepared by a modified coprecipitation methodò, Y Magn. Magn. Mater. Vol-290-291, No. 1, pp. 1442-1445, (2005).

[18] Brockman, F.G., Dowling, P.H., and Steneck, W. G., ñAnomalous behavior of the dielectric constant of a ferromagnetic ferrite at the magnetic Curie point,ò Phys. Rev., Vol-75, No. 9, pp.1440-1440, (1949).

[19] Rose, R.M., Shepard, L.A. and Wulff, J. ñElectronic Propertiesò. New York: Wiley, pp. 258ï 259.

[20] Verway E. J. W. and Haayman, P. W. ñElectronic conductivity and transition point of magnetite (Fe_3O_4)ò, Physica, Vol-8, No. 9 , pp. 979-987, (1941).

[21] Iwauchi, K. ñDielectric properties of fine particles of Fe_3O_4 and some ferritesò, Japan J. of Appl. Phys., Vol-10, pp.1520(1971).

[22] Kolekar, C.B., Kamble, P.N., Kulkarni S.G. and Vaingankar, A. S., ñEffect of Gd^{+3} substitution on dielectric behaviour of copper-cadmium ferritesò, J. Mater. Sci., Vol-30, No. 22, pp. 5784-(1995).

[23] Maxwell, J. ñA treastise on electricity and magnetism,Clarendon Press, Oxford, London, (1982)

[24] Koops, C.G., ñDispersion of resistivity and dielectricconstant of some semiconductors at audio frequencies,ò Phys. Rev., Vol. 83, No.1, pp.121-124(1951).

[25] Kuanr, B.K. and Srivastava, G. ñDispersion observed in electrical properties of semiconductors at audio frequenciesò, J. Appl.Phy. Vol-75, No.10, pp.6115, (1994).

[26] Viswanathan, B. and Murthty, V.R.K., ñIn: Ferrite Materials Science & technologyò, Springer-Verlag Narosa Publishing House, pp. 28-60(2000).

[27] Moulson, A.J. and Herbert, J.M. ñIn: Electroceramicsò, Chapman and Hall, London, 1990, pp. 399.

[28] El-Sayed, A.M., ñElectrical conductivity of nickel-zinc and Cr substituted nickel- zinc ferritesò, Mater. Chem. Phys. Vol-82, No.3, pp.583-587, (2003).

[29] Satyanarayan, R. S., Ramana, S. and Rao, T.S., ñElectrical conductivity of Ni-Zn ferritesò, J. lessï Common Met. Vol-90, No. 2, pp.243-250, (1983).

[30] Van Uitert, L.G. ñdc Resistivity in Nickel and Nickel Zinc Ferrite Systemò, J. Chem. Phys. Vol-23, No-10, pp.1883-1886(1955).

[31] Viswanathan, B. and Murthty, V.R.K., ñIn: Ferrite Materials Science & technologyò, Springer-Verlag Narosa Publishing House, pp. 28-60, (2000).

[32] Moulson, A.J. and Herbert, J.M., ñIn: Electroceramicsò, Chapman and Hall, London, pp. 399, (1990).

[33] Goldman, A., ñModern Ferrite Technologyò 2nd Edition, pp.78-135, (2006).

CHAPTER 5
CONCLUSIONS

The XRD patterns for the polycrystalline $Ba_4Ni_{2-x}Zn_xFe_{36}O_{60}$ (0.0ÒxÒ1.2) compositions confirm the formation of U-type hexaferrites. Lattice parameter increases with increasing of *Zn* content for all compositions. The increase in lattice parameters with increasing *Zn* content can be explained on the basis of the ionic radii. Since the ionic radius of Ni^{2+} is less than that of Zn^{2+} increase in lattice constants with the increase in *Zn* substitution is expected. The microstructural study of the series of $Ba_4Ni_{2-x}Zn_xFe_{36}O_{60}$ hexaferrites shows that the average grain size increases with increase in Zn content. The experimental density of the samples increases and the corresponding porosity of the samples decreases with increasing of Zn content. The initial permeability value increases with increasing Zn content, because the average grain size increase with increasing *Zn* content. It is also observed that the real part of initial permeability, μ_i' of polycrystalline $Ba_4Ni_{2-x}Zn_xFe_{36}O_{60}$ compositions increases with increasing sintering temperature T_s from 1250ºC to 1300ºC and above 1350ºC this decreases. The decreasing trend in permeability μ_i' with frequency is a general phenomenon and is ascribed to the limited speed of spin and domain wall movement in the samples. The real part of initial permeability μ_i' also increases with increasing of sintering temperature, because during the sintering process, the thermal energy generates a force that drives the grain boundaries to grow over pores, thereby decreasing the pore volume and increasing the density of the materials. At a temperature higher than optimum sintering temperature the density decreases, because the intragranular porosity increases as a result of discontinuous grain growth. The discontinuous growth of grain rises with temperature, hindering the migration of the pore to the grain boundary and hence, contributing toward the reduction of the permeability. From the loss factor, the relative quality factor (or *Q* factor) are calculated for all compositions sintered at various temperatures. For inductors used in filter applications, the quality factor is often used as a measure of performance.

From the curve *M-H*, the magnetization as a function of applied magnetic field, it is clear that at room temperature the polycrystalline $Ba_4Ni_{2-x}Zn_xFe_{36}O_{60}$ compositions are in ferrimagnetic state. The saturation magnetization as well as the number of Bohr magnetron, μ_B of the polycrystalline $Ba_4Ni_{2-x}Zn_xFe_{36}O_{60}$ compositions increases with increasing *Zn* content. This can be explained by the fact that the diamagnetic Zn^{2+} cation occupies on the spin-down and tetrahedral sites of T- and S-blocks. In order to explain this lower value of saturation above x=1 can be explained by local spin canting with a magnetic component along the hexagonal c-axis.

The addition of Zn^{2+} ions reduces the dielectric constant in all samples. Zn is volatile in nature and some percentage of it escapes during sintering leaving some vacancies in the structure. The evaporation of Zn ions during sintering, process may increase the number of Fe^{2+} ions at these sites, in turn lead to an increase in hopping conduction. Moreover, the vacant states also may lead to dielectric loss increase in the sample due to increased stress in the lattice. Another phenomenon that dictates the conductivity behavior of the sample is the fact that Zn is known to have strong affinity for tetrahedral site; however, the Ni is present in both octahedral and tetrahedral sites owing to its possible multivalent states. Therefore, a partial substitution of Zn for Ni may dilute conduction effects occurring through tetrahedral sites. Thus, the final conduction behavior in these Zn substituted Ni hexaferrites is a fine balance between all these above mentioned processes.
